# Supporting Information

## An Unconventional Iron Nickel Catalyst for the Oxygen Evolution Reaction

Fang Song,[1,2] Michael M. Busch,[3] Benedikt Lassalle-Kaiser,[4] Chia-Shuo Hsu,[5] Elitsa Petkucheva,[1,6] Michaël Bensimon,[7] Hao Ming Chen,[5,*] Clemence Corminboeuf,[3,*] and Xile Hu[1,*]

[1] Laboratory of Inorganic Synthesis and Catalysis, Institute of Chemical Sciences and Engineering, Ecole Polytechnique Fédérale de Lausanne (EPFL), EPFL-ISIC-LSCI, BCH 3305, Lausanne, CH 1015 Switzerland.

[2] State Key Laboratory of Metal Matrix Composites, School of Materials Science and Engineering, Shanghai Jiao Tong University, Shanghai 200240, China

[3] Laboratory for Computational Molecular Design, Institute of Chemical Sciences and Engineering, and National Center for Computational Design and Discovery of Novel Materials (MARVEL), Ecole Polytechnique Fédérale de Lausanne (EPFL), Lausanne, CH 1015 Switzerland.

[4] Synchrotron SOLEIL, L'Orme des Merisiers, Saint-Aubin, 91191 Gif-sur-Yvette, France

[5] Department of Chemistry, National Taiwan University, Taipei 10617, Taiwan

[6] Department of PEM Hydrogen systems, Acad. E. Budevski Institute of Electrochemistry and Energy Systems (IEES), Acad. G. Bonchev Str. Bl.10, Sofia 1113 Bulgaria.

[7] General Environmental Laboratory, Institute of Environmental Engineering, Ecole Polytechnique Fédérale de Lausanne (EPFL), Lausanne 1015, Switzerland.

# Table of contents

# Supplementary Methods

*Characterization*

SEM images were taken with a Phillips (FEI) XLF-30 FEG scanning electron microscope. EDS-SEM spectra were taken from the spectrometer attached to a Phillips (FEI) XLF-30 FEG scanning electron microscope. XPS measurements were performed on a PHI5000 VersaProbe II XPS system by Physical Electronics (PHI) with a detection limit of 1 atomic percent. Monochromatic X-rays were generated by an Al Kα source (1,4867 eV). The diameter of the analyzed area is 10 μm.

Raman spectra were recorded using a confocal Raman microscope (Renishaw). Spectra were acquired with <0.32 mW of 532 nm laser excitation at the sample surface. The exposure time is 3 s and the 50 spectra were accumulated. For each material, three samples were tested, and for each sample several points were randomly chosen to take Raman spectrum on. For samples after OER, Raman spectra were recorded after chronoamperometry scan at $\eta = 310$ mV for around 10 min. For reference samples, their Raman spectra were similar to those reported in literature works [1-3]).

ICP-MS measurements were conducted on a Finnigan$^{TM}$ element2 high performance high resolution ICP-MS, which consists of a double focusing reverse geometry mass spectrometer. The sensitivity was better than $1.2x10^5$ cps/ppb of $^{115}$In at a mass resolution of 4000, which corresponds to $1.2x10^6$ cps/ppb at low resolution mode of 500. Measurement repeatability expressed in terms of RSD was better than 5%, depending on the element. The accuracy of the method was tested using certified riverine water reference materials SLRS-3. Accuracy was better than 5%. The detection limits obtained for trace metals in the Medium resolution mode (R=4000) without the influence of signal interferences were in routine mode less than 0.2 ng L$^{-1}$ for all elements. Calibration standards were prepared through successive dilutions in cleaned Teflon bottles, of 1g L$^{-1}$ ICP-MS stock solutions (Bernd Kraft). Suprapur® grade nitric acid (65% Merck) was used for the dilution of samples and for the preparation of standards (2+1000). Ultrapure water was produced using Milli-Q® Ultrapure Water System (Millipore, Bedford, USA). The high resolution mode is also useful for samples having unexpected or unknown interferences, because the quantification is obtained by integrating only the area of the analyte peak, without the influence of an unexpected interference peak.

ICP-MS sample preparation: For the testing of Fe concentration in KOH, 1 M KOH solution (Merck KGaA) was neutralized by adding ultrapure nitric acid (65%, Merck KGaA). To test the concentration of Fe on the catalysts surface, NF-AC-NiO$_x$-Fe (electrode area: 1.0-1.1 cm$^2$) was dipped in ultrapure nitric acid (mixture of 0.25 mL ultrapure nitric acid (65%, Merck KGaA) and 5 mL H$_2$O) for 1-2 min, washed with distilled water twice. Dipping in nitric acid for a longer time led to same results. All the nitric acid and washing water were collected. Water was then added to reach the total volume of 10 mL. To make sure all the surface Fe was dissolved in nitric acid, the treated samples were checked by testing the OER activity in Fe free 1M KOH. The OER activity is similar to NF-AC in Fe-free 1M KOH, indicating the total dissolution of surface Fe. The loading examined in this method is also close to the value calculated from the Fe concentration change before and after 100 CVs activation of NF-AC in 1M KOH (60 mL). This confirmed the total dissolution of Fe on NF-AC-NiO$_x$-Fe surface. To be consistent with literature data, the loadings were referred to iron oxide, assuming a Fe$_2$O$_3$ formula. A variation in the formula will only introduce negligible uncertainty in the comparison.

*Calculation of the specific current density, J$_s$:*

AC impedance measurements were taken over the frequency range of 100 Hz to 0.1 kHz. Impedance measurements were taken on charged catalysts at 0.501, 0.481 and 0.461 V versus

Ag/AgCl.[4] The double-layer capacitance values ($C_{dl}$) were obtained through fitting of the impedance spectrum using an equivalent circuit (Voigt circuit, see below) with two characteristic time constants[5].
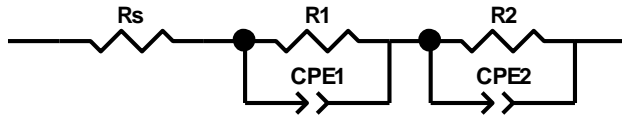


The electrochemically active surface area (ECSA) was calculated from the double-layer capacitance according to the equation below:

$$ECSA = C_{dl}/C_s$$

Where $C_s$ is the specific capacitance. $C_s$ is 81 uF cm$^{-2}$ for Ni(Fe)O$_x$ [4].

The roughness factor (RF) was calculated by taking the estimated ECSA and dividing it by the geometric area of the electrode (normally 1 cm$^2$). The specific current density $J_s$ was calculated according to equation below:

$$J_s = J/RF$$

Where $J$ is the geometric current density.

### Calculation of $J_s$ of NiFeO$_x$ from data in the literatures [4, 6]:

The NiFeO$_x$ sample obtained by continuous deposition and described in a recent paper[4] was chosen as a state-of-the-art sample. At the loading of 300 nmol of metal per cm$^{-2}$, the TOF is ca. 0.18 s$^{-1}$. So the geometric current density is

$J$ = TOF * 4 n F = 0.18 s$^{-1}$ x 4 x (300 x 10$^{-9}$) mol.cm$^{-2}$ x 96485 C mol$^{-1}$= 0.0208 A.cm$^{-2}$ = 20.8 mA.cm$^{-2}$

At the loading of 300 nmol of metal per cm$^{-2}$, the capacitance $C_{dl}$ is ca. 20 mF.cm$^{-2}$.

The roughness (RF) is therefore

RF = $C_{dl}/C_s$= 20 mF.cm$^{-2}$/0.081 mF.cm$^{-2}$= 247 (taking Cs as 0.081 mF.cm$^{-2}$, which is the value we used to calculate the RF for our reference NiFeO$_x$ samples)

$J_s$ = J/RF = J/247 = 0.084 mA.cm$^{-2}$.

This value is similar to the one determined in the current work (0.13±0.02 mA.cm$^{-2}$) for the reference NiFeO$_x$ sample on GC.

For another state-of-the-art sample of NiFeO$_x$ [6], the $J_s$ was reported at an overpotential of 350 mV: $J_{s,\eta=0.35 V}$ = 3 ± 2 mA cm$^{-2}$. Considering a Tafel slope of 35 mV/dec, the $J_s$ at 300 mV is $J_{s,\eta=0.30 V}$ = 0.11 ± 0.07 mA cm$^{-2}$, which is again similar to the value determined in the current study (0.13±0.02 mA cm$^{-2}$).

### Calculation of Turnover frequency (TOF)
The TOF value was calculated from the equations:

$$TOF = \frac{J \times A}{4 \times F \times m}$$

where $J$ is the current density at a given overpotential (e.g. $\eta = 250$, 270, and 300 mV), $A$ is the geometric surface area of the electrode, $F$ is the Faraday constant ( a value of 96485 C mol$^{-1}$), and $m$ is the number of moles of Fe on the electrode. For our samples, the Fe loadings are measured by ICP-MS.

Figure S2b shows the potential-dependent TOFs for five electrodes with an iron oxide loading of 1.0-14.1 μg cm$^{-2}$. Table S1 gives the TOFs of 11 individual electrodes. Except at the lowest loading, i.e, 1.0 μg cm$^{-2}$, the TOFs of samples with different loadings in this range are similar. The TOFs at 1.0 μg cm$^{-2}$ are significantly higher, in agreement with recent observations that at an ultralow loading ($\leq 1$ μg cm$^{-2}$) the TOFs of certain OER catalysts were abnormally high compared to the same catalysts at loadings between 1.4 to 14.1 μg cm$^{-2}$. A "substrate effect"[7] or "nucleus sintering" [8] was invoked to rationalize these observations. The intrinsic activity, however, is best represented by TOFs at higher loadings [8].


*XAS Data collection.*
Ex-situ XANES data were collected on the LUCIA beamline of SOLEIL [9], at an energy of 2.75 GeV and with a ring current of 100 mA (8-bunch mode). The incident beam energy was monochromatized using a Si 111 double crystal monochromator. The electrochemical *in-situ* XAS were recorded at SP8 (Japan) 12B2 Taiwan beamline of National Synchrotron Radiation Research Center (NSRRC), the electron storage ring was operated at 8.0 GeV with a constant current of ~100 mA. The *in-situ* XAS measurement was performed at the desired voltage to keep the situation of reduction with a special cell designed for these experiments. The photon energy was calibrated with the first inflection point of Fe K-edge and Ni K-edge in Fe and Ni metal foils, respectively. XAS data were collected in either total electron yield mode or fluorescence mode.


*XAS data analysis and EXAFS fittings.*
The data collected were normalized to the incoming incident photon flux and processed with the Athena software from the IFEFFIT package. $E_0$ values of 7112.0 eV and 8333.0 eV were used to calibrate all data with respect to the first inflection point of the absorption K-edge of either iron or nickel foil, respectively.
EXAFS curve fitting was performed with Artemis and IFEFFIT software using *ab initio-* calculated phases and amplitudes from the program FEFF 8.2 [10, 11]. These *ab initio* phases and amplitudes were used in the EXAFS equation:

$$\chi(k) = S_0^2 \sum_j \frac{N_j}{kR_j^2} f_{eff_j}(\pi,k,R_j) e^{-2\sigma_j^2 k^2} e^{-2R_j/\lambda_j(k)} \sin(2kR_j + \phi_i(k))$$

The neighboring atoms to the central atom(s) are divided into $j$ shells, with all atoms with the same atomic number and distance from the central atom grouped into a single shell. Within each shell, the coordination number $N_j$ denotes the number of neighboring atoms in shell $j$ at a distance of $R_j$ from the central atom. $f_{eff_j}(\pi,k,R_j)$ is the *ab initio* amplitude function for shell $j$, and the Debye-Waller term $e^{-2\sigma_j^2 k^2}$ accounts for damping due to static and thermal disorder in absorber-backscatterer distances. The mean free path term $e^{-2R_j/\lambda_j(k)}$ reflects losses due to

inelastic scattering, where $\lambda_j(k)$ is the electron mean free path. The oscillations in the EXAFS spectrum are reflected in the sinusoidal term $\sin(2kR_j + \varphi_{ij}(k))$, where $\varphi_{ij}(k)$ is the *ab initio* phase function for shell *j*. $S_0^2$ is an amplitude reduction factor due to shake-up/shake-off processes at the central atom(s). The EXAFS equation was used to fit the experimental data using CN, R, and the EXAFS Debye-Waller factor (DW; $\sigma^2$) as variable parameters. For the energy (eV) to wave vector ($k$, Å$^{-1}$) axis conversion, the $S_0^2$ value was determined as 0.90. All fits were performed in the R space. The R-value (%) is employed to judge whether a fitting is proper, and is expressed by the following equation:

$$\boldsymbol{R} = \Sigma\{k^n\chi_{obs}(k) - k^n\chi_{cal}(k)\}^2/\Sigma\{k^n\chi_{0bs}(k)\}^2$$

# Computational Details

All computations were performed using the GPAW code [16,17] in combination with the Atomic Simulation Environment (ASE) (https://wiki.fysik.dtu.dk/ase/). The RPBE[18] exchange correlation functional together with a 0.17 Å grid spacing and a 1x5x1 k-point set for γ-FeOOH or a 5x5x1 k-point set for γ-NiOOH was used. $H_2O$ and $H_2$ were modeled using only the Γ-point. The core electrons were approximated through Projector Augmented Wavefunctions (PAW)[19]. A smearing of 0.1 eV was added to facilitate the convergence of the wavefunction. Following previous work[20], the spin was treated explicitly assuming a high-spin configuration on Fe and a low spin configuration on Ni. Ferromagnetic coupling between the ions was used. Assuming a ferromagnetic coupling reduces the complexity of the computation significantly while only introducing a minor additional error bar. Assuming a Neel temperature of 1000 K the uncertainty between the assumed and real magnetic coupling would correspond to an additional error of approximately 0.1 eV. This procedure has been applied successfully to a large number of materials.[20,21]. The geometries were optimized using the BFGS algorithm and convergence was assumed if the forces were below 0.05 eV/Å. The final redox potentials and adsorption potentials were computed using the theoretical Normal Hydrogen Electrode described by Rossmeisl *et al.*[22,23] assuming a constant set of corrections for Zero-point energies and entropy effects.

γ-NiOOH and γ-FeOOH were modeled in independent unit cells. Both compounds display a brucite type crystal structure. γ-FeOOH model is obtained by cutting the lattice along the (010) plane. A 4-monolayer slab with 2 monolayers being fixed to bulk positions in combination with a 2x1 surface is used. A vacuum of 14 Å along the x-axis and 9 Å along the z axis is added to avoid interactions between the slabs. γ-Ni(OH)$_2$ and γ-NiOOH were modeled using a single layer assuming oxidation and reduction of threefold M-OH and M=O species. γ-NiOOH edge and corner sites as well as NiO were excluded based on their high redox potentials reported in literature [12,13]. No significant changes of the geometry were observed during relaxation. Following the state–of-the-art procedure in computational electrochemistry [14] solvent and double layer effects were neglected. This procedure is known to semi-quantitatively reproduce experimental trends [12,13,15,16].

The computational normal hydrogen electrode uses water in the gas phase as reference. The influence of solvation can be estimated by assuming a suitable Born-Haber cycle. In this Born-Haber cycle, the transfer of one water molecules from bulk solution into gas phase costs approximately 0.4 eV.[17] Assuming the above numbers one gains 0.3 eV for *OH (1 water molecule needed) and 0.6 eV for *OOH (2 water molecules needed). Thus, no significant shifts in the overpotential and binding energies is expected due to cancellation of errors. This is in line with recent calculations by Calle-Vallejo et al. which show that solvation has no influence on the scaling relations between OH an OOH.[18]

All calculations have performed using a pure GGA functional without Hubbard U correction. This choice can be justified considering the problematic electronic structures of transition metal compounds. Any calculation considering these materials will essentially suffer from errors resulting from static and dynamic correlation. The self-interaction error is especially severe for highly localized systems such as transition metal complexes[19] and can be corrected by adding exact exchange to the functional or using a Hubbard U correction. In the case of NiOOH and FeOOH, however, a certain degree of delocalisation is expected. Thus, a pure GGA functional is not necessarily problematic. Indeed, previous calculations show good agreement between overpotentials obtained experimentally and computed using a pure GGA functional.[13] Errors from static correlation on the other hand are a result from the inability of single determinant methods (such as DFT) to correctly describe the wave function. The degree of

multi-reference character unfortunately not only depends on the material but unfortunately also varies with the adsorbate.[19] Thus, a Hubbard U correction, which is typically determined for a bulk propertiy such as the band gap, is likely unable to correctly describe the detailed balance between the two errors.

In agreement with current high level publications in the field [12, 13, 15, 16], we limited our computations to a "thermodynamic only" picture. This is due to the fact that activation barriers in electrocatalysis can be expected to be strongly influenced by the detailed structure of the double layer. This is especially true for reaction steps comprising the abstraction or transfer of $H^+/e^-$ couples. Additionally, both the mono-nuclear and bi-functional formation of the O-O bond bears significant mechanistic similarities. In both cases a nucleophile (OH$^-$ or H$_2$O) attacks a Fe=O unit. Indeed, the superiority of the bi-functional mechanism lies not in differences in the details of the O-O bond formation step but in the ability to form a thermodynamically more favorable final state via H-transfer to an acceptor species. Thus, assuming a negligible O-O bond formation barriers for both mechanisms, the "thermodynamic only" is able to capture the differences between both reaction paths. Moreover, it has been shown that the potential limiting kinetic barriers for OER on a number of active metal oxides such as G-FeCoW and NiFeO$_x$ are small compared to thermodynamics (less than 1 eV) [14].

The eq. 5 in the main text is a simplification of two nearly simultaneous steps: first, *=O + OH$^-$ + A → *-O$_2^-$ + e$^-$ + A-H$^+$; then internal electron transfer: *-O$_2^-$ + A-H$^+$ → *-O$_2$ + A-H. The simplification was necessary because the DFT functionals employed here cannot be used to compute charged systems. Moreover, the computations of *-O$_2$ are problematic by DFT due to the multi-reference problem. Thus, eq. 5 is used for this step. The overall thermodynamic picture should be the same.

### Construction of Volcano Plot

In the volcano plot, the redox potential of the oxidation form M-OH to M=O is used as a descriptor. To construct a volcano plot, linear scaling relations between the water oxidation intermediates M-OH, M=O and M-OOH are required. Following previous work [13, 17], we assume:

$$\Delta G(M = O) = 2\Delta G(M - OH) \qquad \text{(Equation S1)}$$

$$\Delta G(M - OOH) = \Delta G(M - OH) + 3.2eV \qquad \text{(Equation S2)}$$

Water and hydrogen are taken as reference states, i.e.

$$G(H_2O) = G(H_2) = 0eV \qquad \text{(Equation S3)}$$

and the experimental values of 4.92 eV is used for oxygen.

$$G(O_2) = 4.92eV \qquad \text{(Equation S4)}$$

a) Mono-nuclear mechanism:

At the strong binding side (left slope in Figure S5a), the formation of the O-O bond is potential determining:

$$M = O + H_2O \rightarrow M - OOH + H^+ + e^- \qquad \text{(Equation S5)}$$
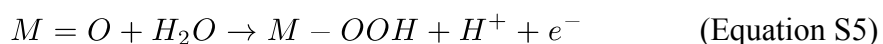
Subtracting the overpotential of 1.23 eV from the reaction energy one obtains:

$$-\eta_1 = -\{[\Delta G(M - OOH) - \Delta G(M = O)] - 1.23eV\} \qquad \text{(Equation S6)}$$

Inserting equation S2, the theoretical overpotential becomes

$$-\eta_1 = [\Delta G(M = O) - \Delta G(M - OH)] - 1.97 eV \qquad \text{(Equation S7)}$$

At the weak binding side (right slope in Figure S5a), the overpotential is determined by the oxidation of M-OH to M=O.

$$M - OH \rightarrow M = O + H^+ + e^- \qquad \text{(Equation S8)}$$
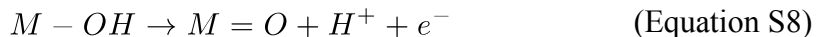
Accordingly, the overpotential is given by

$$-\eta_2 = -[\Delta G(M = O) - \Delta G(M - OH)] + 1.23 eV \qquad \text{(Equation S9)}$$

b) Bi-functional Mechanism

The bi-functional mechanism only influences the energetics of the O-O bond formation step. Accordingly, the weak binding side is given by equation S9. At the top of the volcano the recovery of the hydrogen acceptor unit $Ni_3$-O determines the overpotential.

$$Ni_3 - OH \rightarrow Ni_3 - O + H^+ + e^- \qquad \text{(Equation S10)}$$
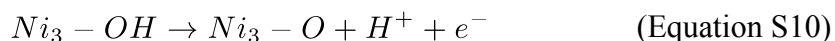
Since this step is independent of the descriptor the top becomes a flat line. With

$$\Delta G(Ni_3 - OH \rightarrow Ni_3 - O) = 1.3 eV \qquad \text{(Equation S11)}$$

the overpotential becomes:

$$-\eta_3 = -0.07 eV \qquad \text{(Equation S12)}$$

The strong binding side is replaced by the bi-functional formation of the O-O bond:

$$M = O + Ni_3 - O + H_2O \rightarrow M + O_2 + Ni_3 - OH + H^+ + e^- \qquad \text{(Equation S13)}$$
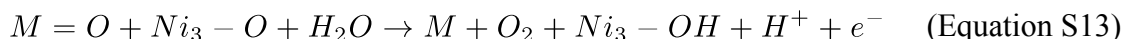
the corresponding theoretical overpotential can then be obtained through

$$-\eta_4 = -\{[G(O_2) + G(Ni_3 - OH)] - \Delta G(M = O) + G(Ni_3 - O)] - 1.23\} \qquad \text{(Equation S14)}$$

According to equation S1, the energetics of the reaction step M-OH to M=O is equivalent to $\Delta G$(M-OH). Inserting also $\Delta G(O_2)$ from equation S4 and $\Delta G(Ni_3$-OH$\rightarrow Ni_3$-O) from equation S11 gives:

$$-\eta_4 = 2[\Delta G(M = O) - \Delta G(M - OH)] - 2.39 \qquad \text{(Equation S15)}$$

***Zero-point Energy and Entropy Corrections***

| Reaction | ZPE + T$\Delta$S [eV] |
|---|---|
| M + H$_2$O → M-OH + 0.5 H$_2$ | 0.4 |
| M + H$_2$O → M=O + H$_2$ | 0.05 |
| M + 2 H$_2$O → M-OOH + 1.5 H$_2$ | 0.41 |

ZPE and T$\Delta$S corrections according to reference [13].

*Summary of Binding Energies*

| System | $\Delta G(M\text{-}OH)$ [eV] | $\Delta G(M{=}O)$ [eV] | $\Delta G(M\text{-}OOH)$ [eV] |
|---|---|---|---|
| $\gamma$-FeOOH (010) | 1.10 | 2.34 | 4.02 |

*Redox Potentials of Hydrogen Acceptors*

| Hydrogen Acceptor | $\Delta G$ [eV] |
|---|---|
| $Ni^{2+}_3\text{-}OH \rightarrow Ni^{3+}_3{=}O$ (*) | 1.2 |
| $Ni^{2+}_3\text{-}OH \rightarrow Ni^{3+}_3{=}O$ (**) | 1.3 |

(*) in $Ni^{2+}$ embedding (**) in $Ni^{3+}$ embedding
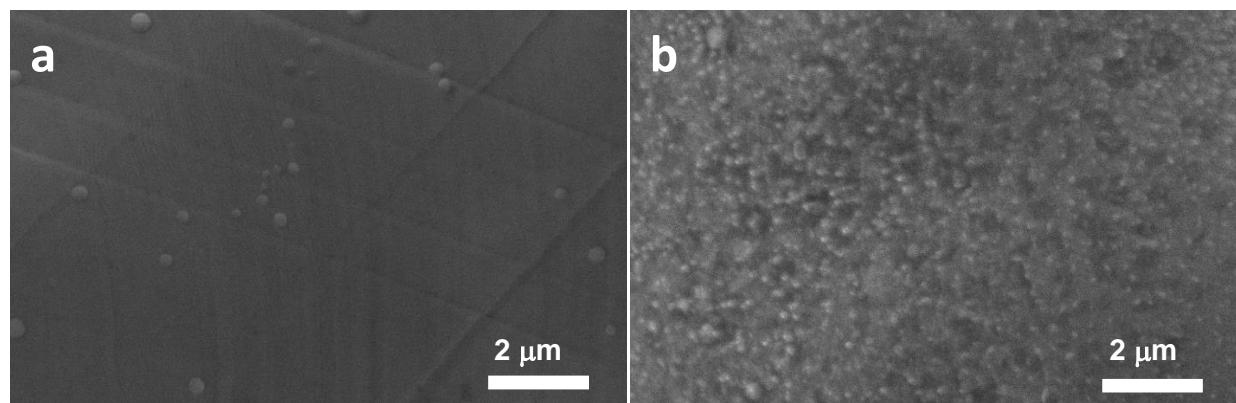
**Figure S1.** SEM images of the surfaces of (a) NF and (b) NF-AC.
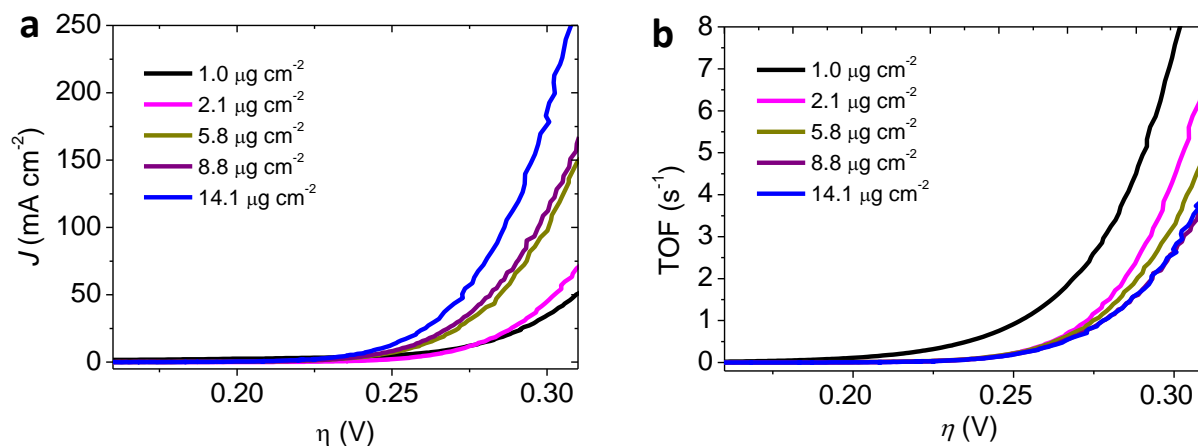
**Figure S2.** (a) Polarization curves and (b) corresponding TOFs of five representative NF-AC-NiO$_x$-Fe electrodes; TOFs were calculated according to the total amount of Fe ions measured by ICP-MS. Backward scan; Scan rate: 1 mV s$^{-1}$; IR corrected. Except at the lowest loading, i.e, 1.0 μg cm$^{-2}$, the TOFs of samples with different loadings in this range are similar. The TOFs at 1.0 μg cm$^{-2}$ are significantly higher, in agreement with recent observations that at an ultralow loading ($\leq$ 1 μg cm$^{-2}$) the TOFs of certain OER catalysts were abnormally high compared to the same catalysts at loadings between 1.4 to 14.1 μg cm$^{-2}$. A "substrate effect"[7] or "nucleus sintering"[8] was invoked to rationalize these observations. The intrinsic activity, however, is best represented by TOFs at higher loadings[8].
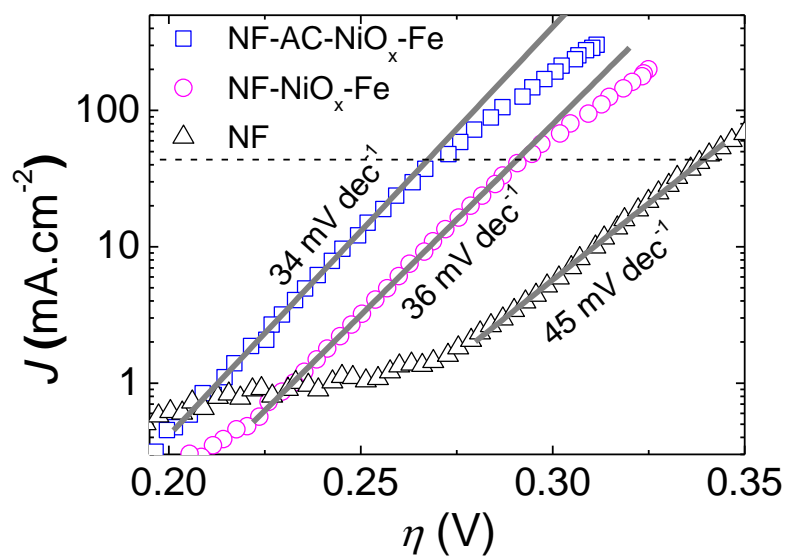
**Figure S3.** Tafel plots of NF, NF-NiO$_x$-Fe and NF-AC-NiO$_x$-Fe. The Tafel plots for NF-NiO$_x$-Fe and NF-AC-NiO$_x$-Fe are based on the 1$^{st}$ LSV after 100 CVs' activation. The Tafel plot of NF is based on the 1$^{st}$ LSV before 100 CV's activation. The loading of Fe in NF-AC-NiO$_x$-Fe is 14.1 µg cm$^{-2}$, and in NF-NiO$_x$-Fe is 4.3 µg cm$^{-2}$. The deviation of experimental data from the Tafel line above η = 300 mV indicates the influence of mass transport.
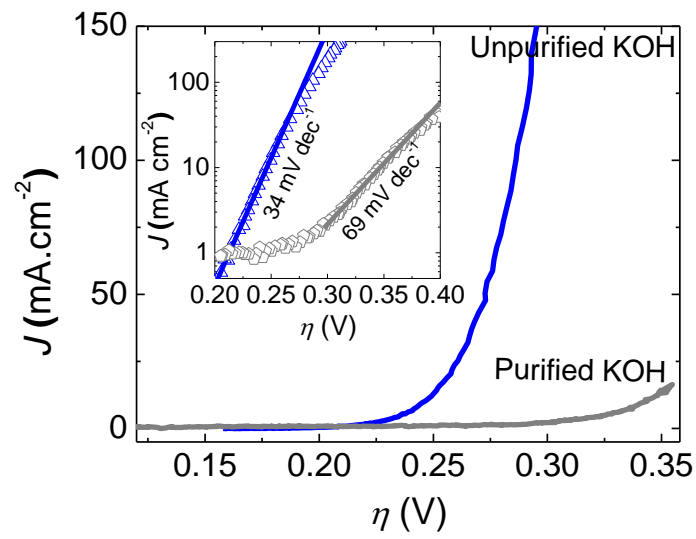
**Figure S4.** Polarization curves of NF-AC activated in unpurified KOH and purified KOH (Fe-free). Backward scan; Scan rate: 1 mV s⁻¹; IR corrected. The inset shows the corresponding Tafel plots.
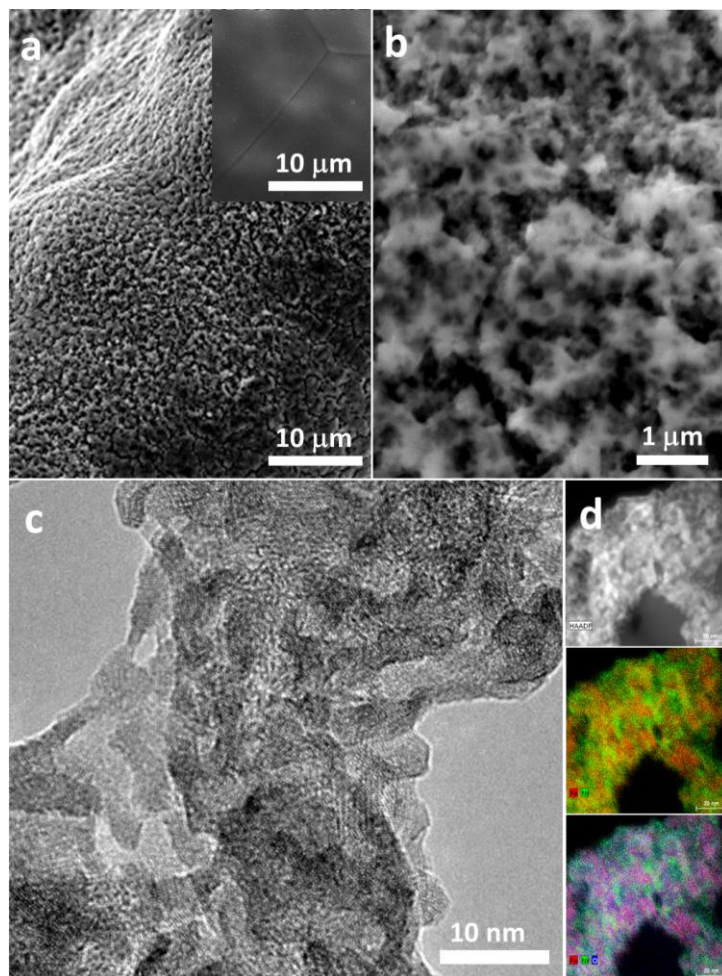
**Figure S5.** Characterization of NF-AC-FD. (a, b) SEM images; (c) TEM images. The inset in (a) shows the SEM image of NF-AC. (d) HAADF and corresponding elemental mapping images of the surface layer. Color codes: red for Fe; green for Ni; blue for O; purple for the mixture effect of Fe and O.
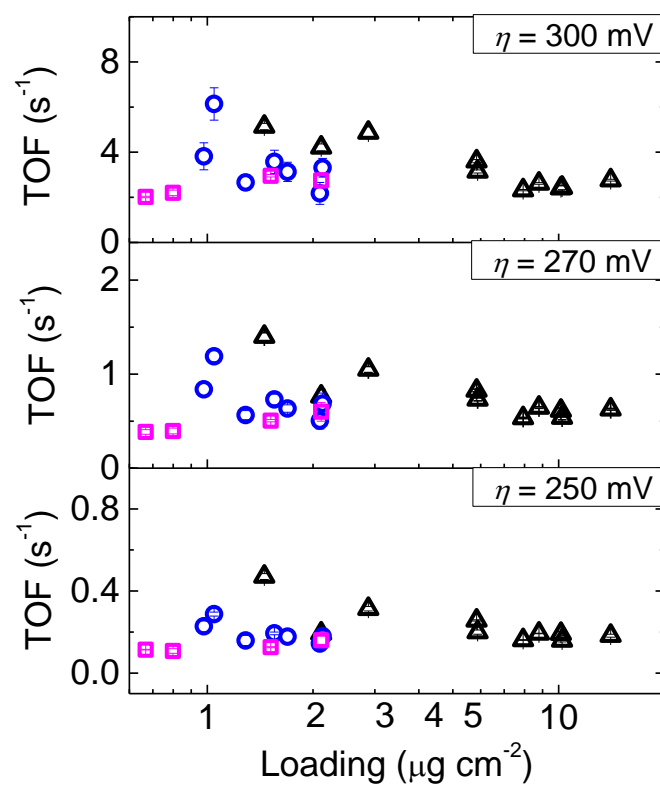
**Figure S6.** The TOFs at different loadings of iron (expressed as $Fe_2O_3$) for NF-AC-$NiO_x$-Fe (black triangles), Au-$NiO_x$-Fe (blue spheres) and GC-$NiO_x$-Fe (magenta rectangles).
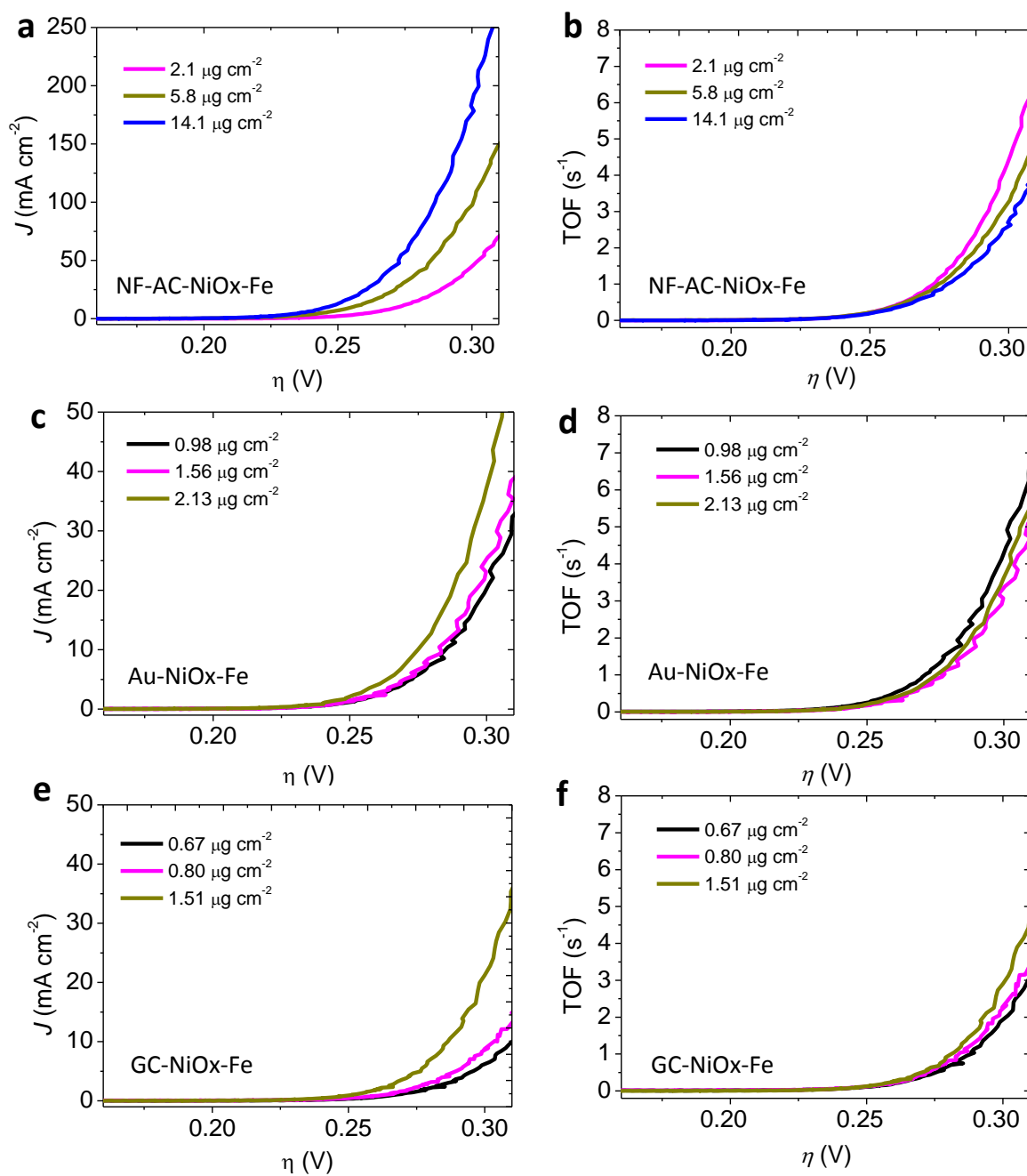
**Figure S7.** Polarization curves and corresponding TOFs of three representative samples. (a, b) NF-AC-NiO$_x$-Fe; (c, d) Au-NiO$_x$-Fe; (e, f) GC-NiO$_x$-Fe. TOFs were calculated according to the total amount of Fe ions measured by ICP-MS. Backward scan; Scan rate: 1 mV s$^{-1}$; IR corrected.
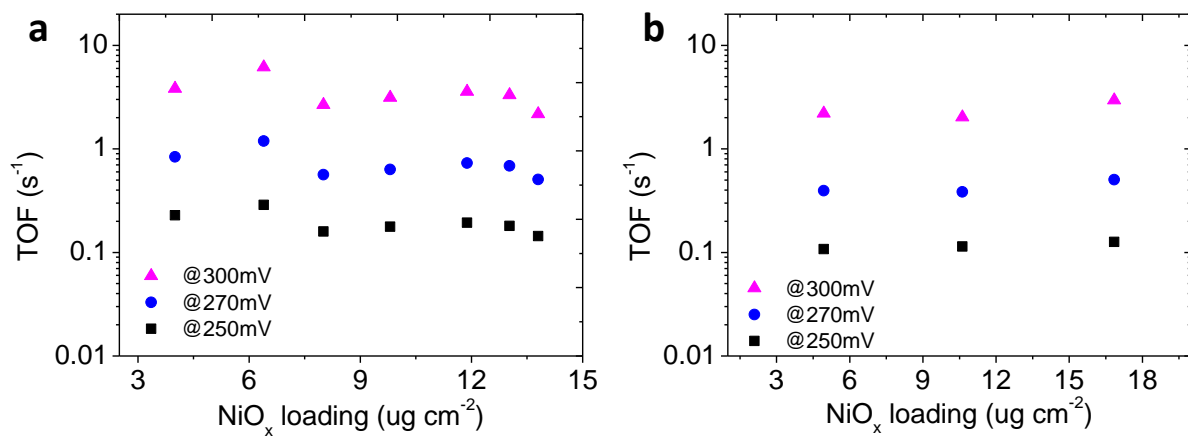
**Figure S8.** TOFs at different loadings of $NiO_x$. (a) $Au\text{-}NiO_x\text{-}Fe$; (b) $GC\text{-}NiO_x\text{-}Fe$.
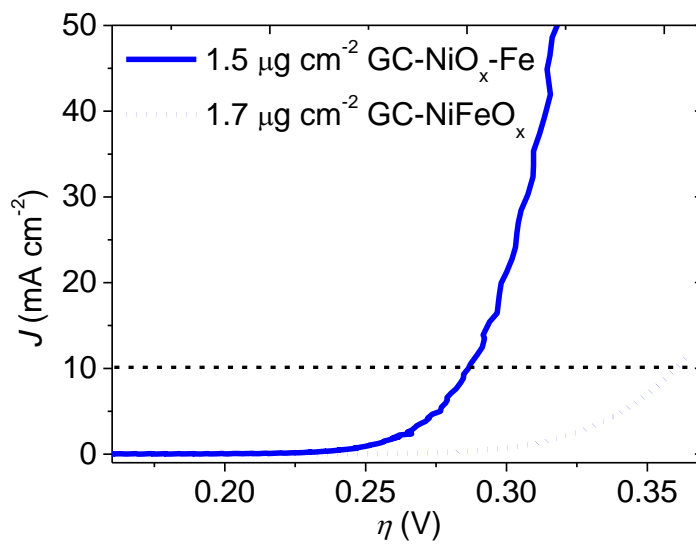
**Figure S9.** Comparison of polarization curves between GC-NiO$_x$-Fe and GC-NiFeO$_x$ at a similar loading.
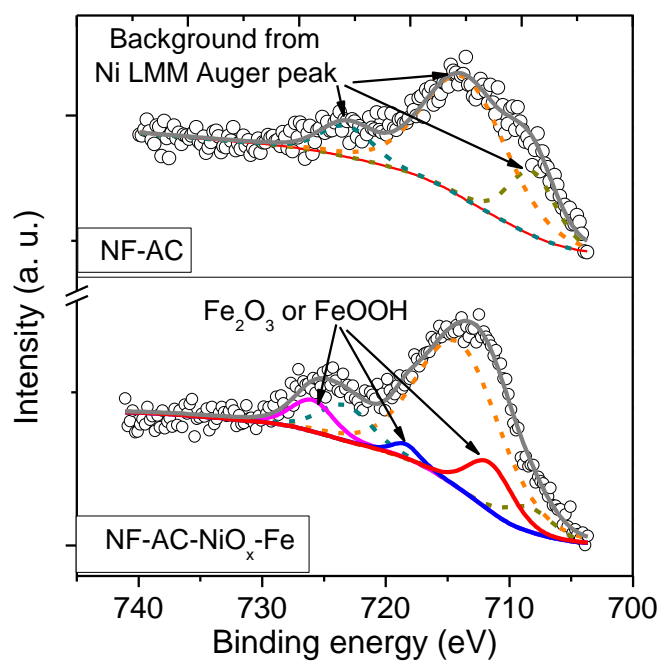
**Figure S10.** High resolution Fe 2p XPS spectra of NF-AC and NF-AC-NiOx-Fe. The Fe 2p spectral background has contribution from Ni LMM Auger peaks [20, 21]. After deduction of the background from Ni LMM Auger peaks, three residual peaks (711.5, 719.0 and 725.9 eV) in NF-AC-NiO$_x$-Fe can be ascribed to iron oxides deposited on the nickel foam. Due to similarities in the binding energies and spectral shapes of the higher oxides of iron, it is not possible to assign the iron species to Fe$_2$O$_3$ or FeOOH using XPS [22, 23].
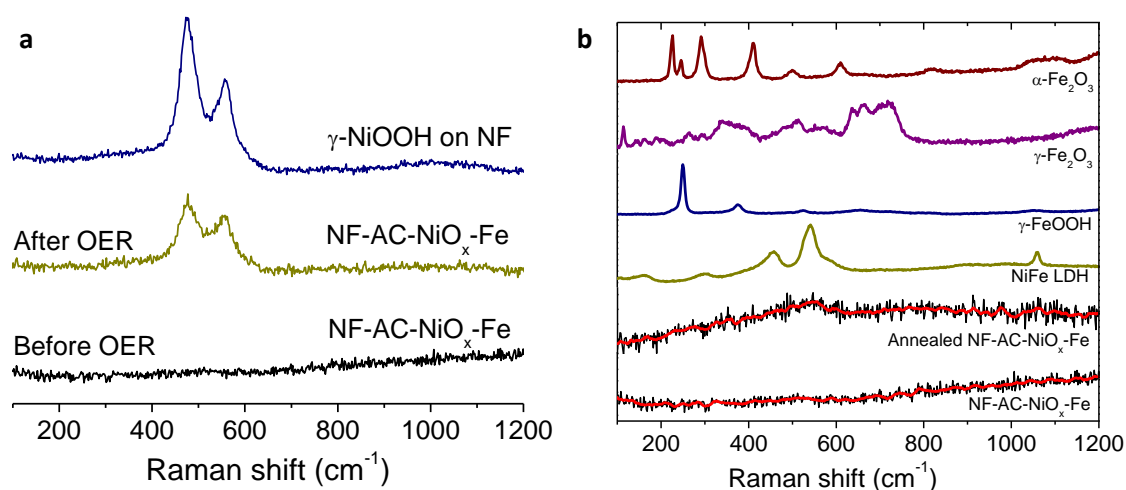
**Figure S11.** Raman spectra. (a) NF-AC-NiO$_x$-Fe (before OER and after OER) and γ-NiOOH on NF. (b) NF-AC-NiO$_x$-Fe, annealed NF-AC-NiO$_x$-Fe, and reference samples of NiFe LDH, γ-FeOOH, γ-Fe$_2$O$_3$, and α-Fe$_2$O$_3$. Because γ-NiOOH has a lifetime of 1 h at an open circuit, the Raman data, collected immediately before and after the catalytic test, reveal that the NiO$_x$ component of the catalyst exists as γ-NiOOH at OER potentials. As for the iron oxide species, no characteristic peaks of crystalline hematite (α-Fe$_2$O$_3$), maghemite (γ-Fe$_2$O$_3$), lepidocrocite (γ-FeOOH), or NiFe layered double hydroxide (LDH; structurally related to Fe-doped γ-NiOOH) were observed in the Raman spectrum of the as-prepared catalyst, before or after OER. This is likely due to the low concentration of the iron oxide species.
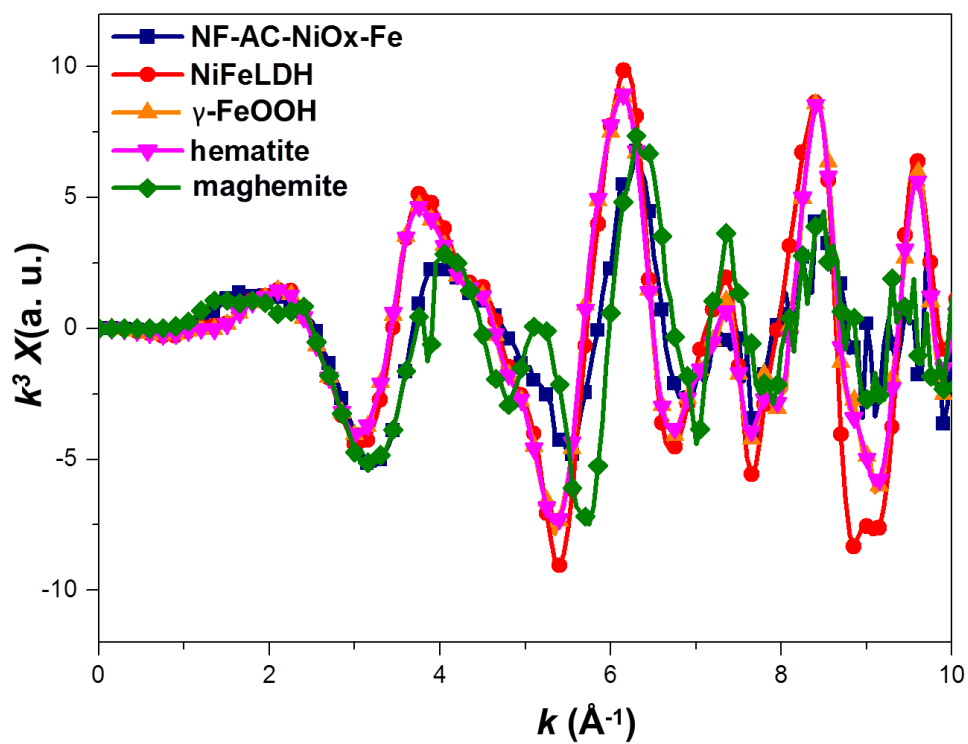
**Figure S12.** EXAFS Fe K-edge k-space spectra of NF-AC-NiO$_x$-Fe and relevant references.
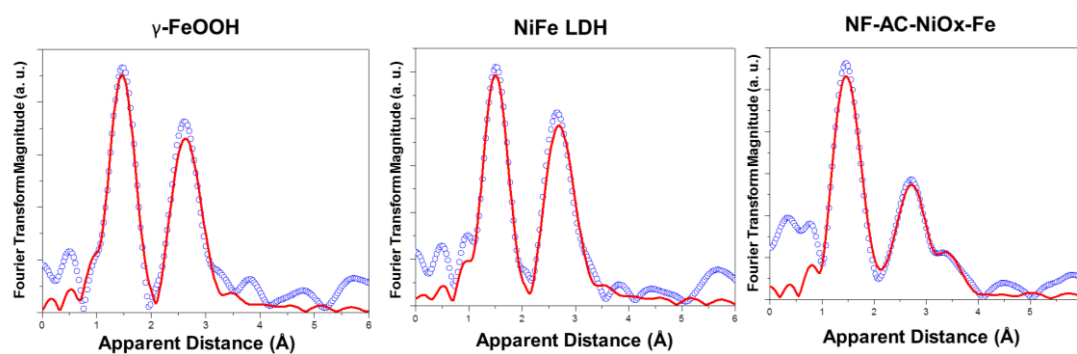
**Figure S13.** EXAFS Fe K-edge r-space spectra of γ−FeOOH, NiFe LDH and NF-AC-NiO$_x$-Fe samples extracted from EXAFS refinement, experimental data (blue circle) and the corresponding fit (red). Fitting parameters are gathered in Table S10.

**Without Fe-Ni (outside) path**
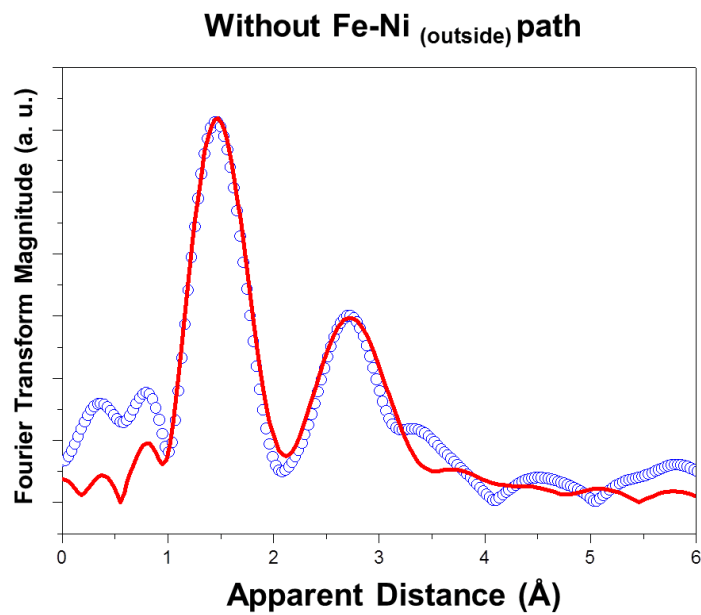


**Figure S14.** EXAFS Fourier transform Fe K-edge spectra of NF-AC-NiO$_x$-Fe (blue circle) and the corresponding fit (red) without Fe-Ni (outside) path. These fittings indicate that a good fitting cannot be realized without Fe-Ni$_{(outside)}$ path.
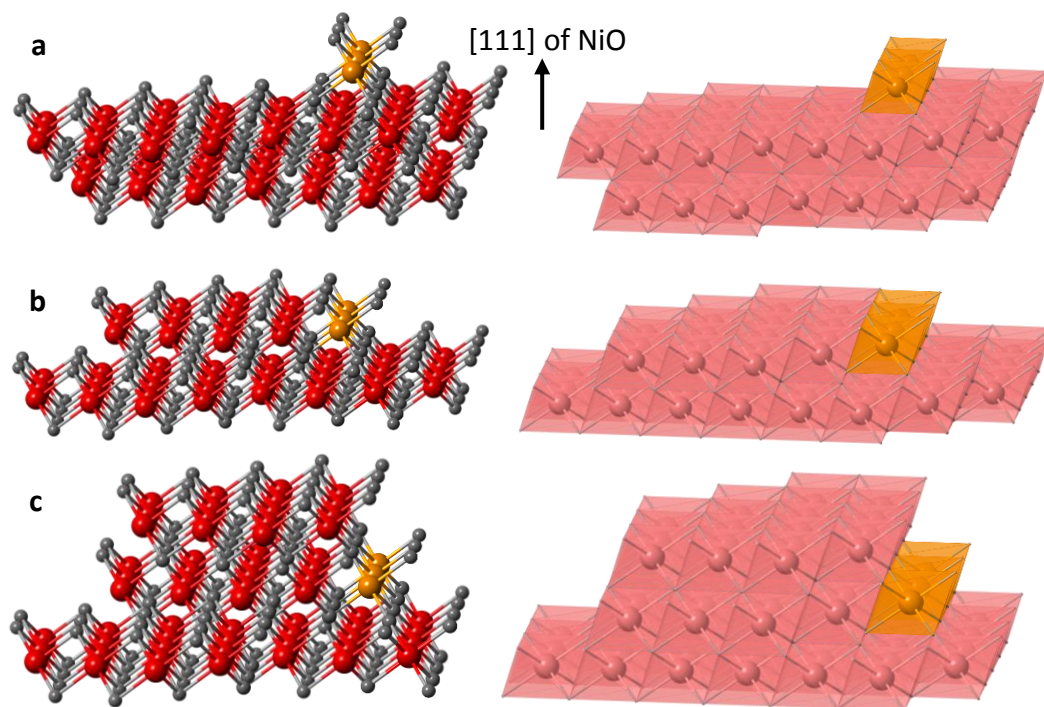
**Figure S15.** Structure models of the dry catalyst. (a) Fe located at the surface, (b) Fe located on the step I, (c) Fe located on the step II. (left) ball-stick structures and (right) polyhedral structures.
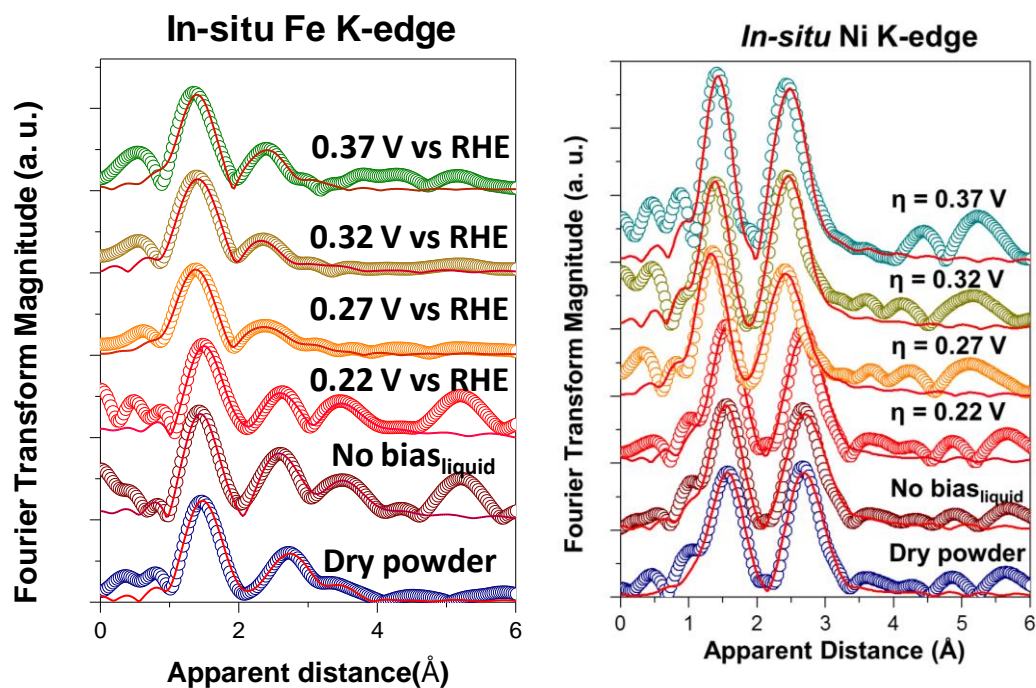
**Figure S16.** Fe and Ni K-edge EXAFS spectra (R-space) measured under operando conditions for the Au-NiO$_x$-Fe sample (experimental data; color circle) and the corresponding fittings (red). Fitting structural parameters are gathered in Table 2 and Table S11.
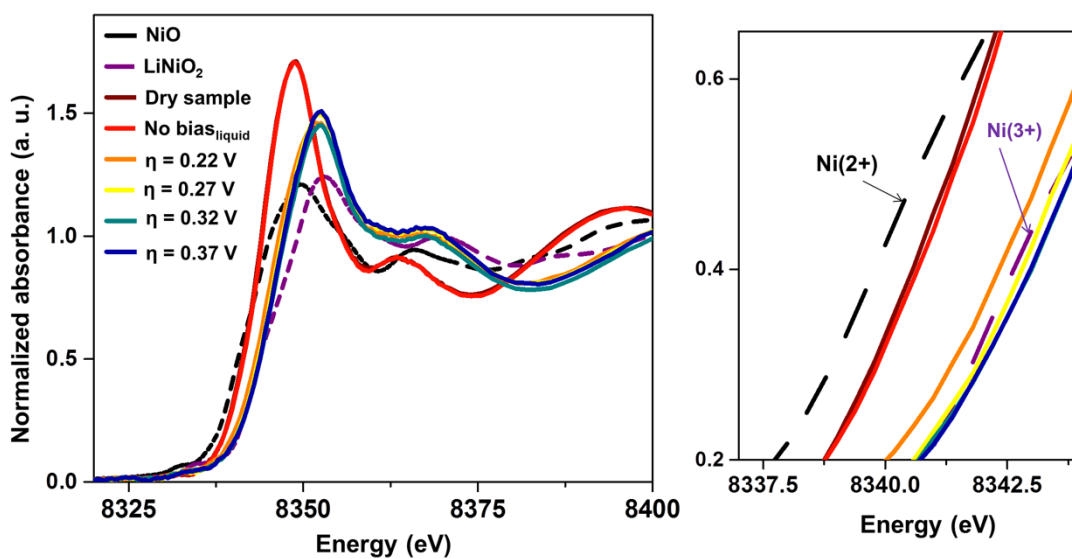
**Figure S17.** Operando XANES spectra of Ni K-edge for Au-NiOx-Fe sample and the corresponding references, showing that the oxidation states of as-prepared sample in dry condition and in electrolyte (without bias) are close to +2. Once the potential is further increased to launch the OER, the oxidation states approach +3 and even higher. Ni(2+) refers to NiO, and Ni(3+) refers to $LiNiO_2$.

a  [111] of NiO    OER    [001] of NiOOH

b  OER

c  OER
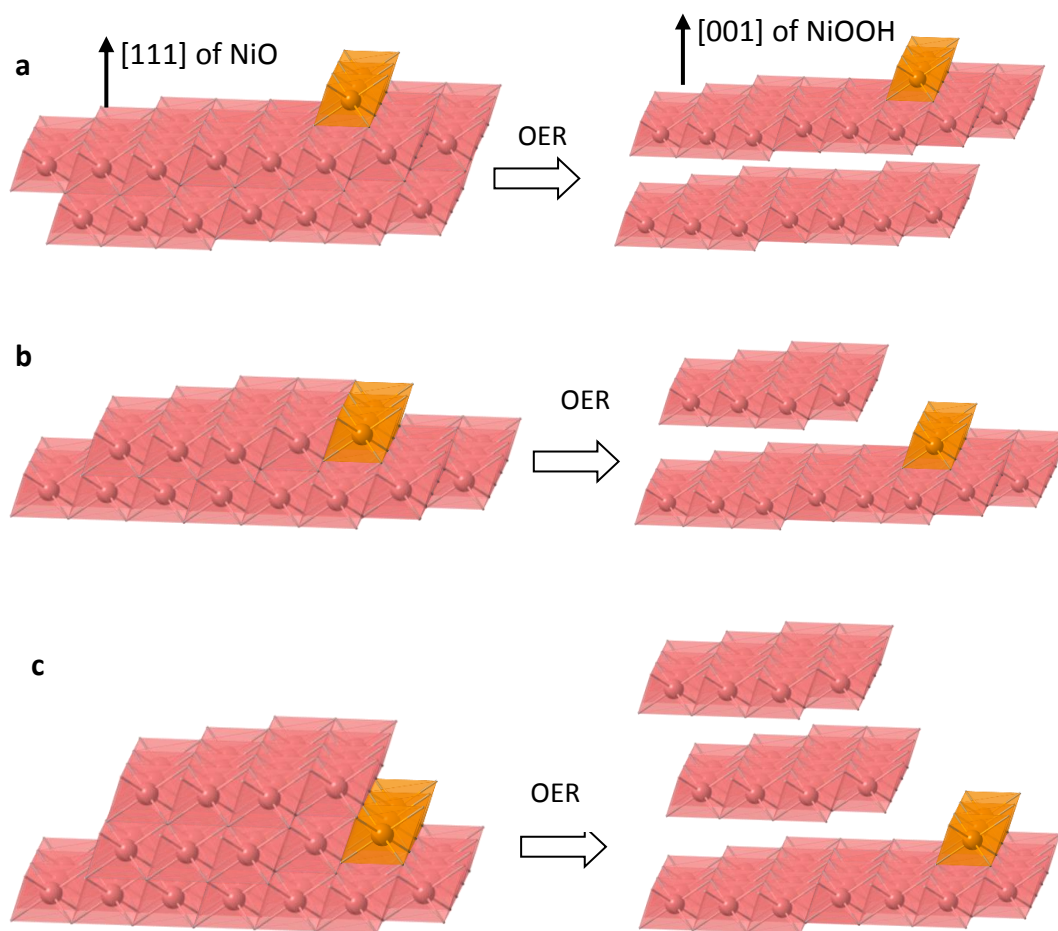
**Figure S18.** Structural transformation during OER. (a) Fe located on the surface, (b) Fe located on the step I, (c) Fe located on the step II.
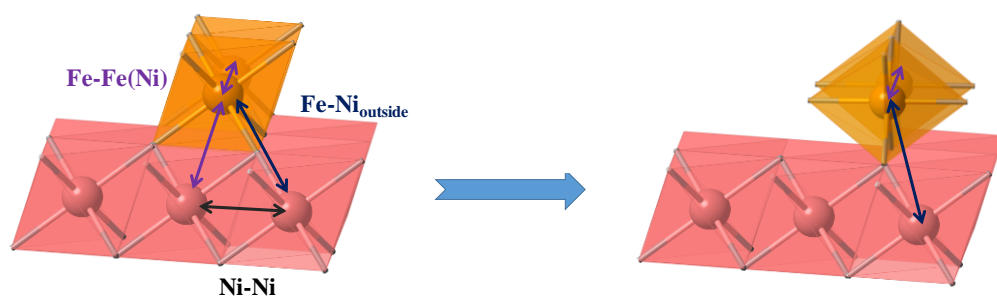
**Figure S19.** FeO$_6$ octahedrons tilt on the NiOOH under OER condition
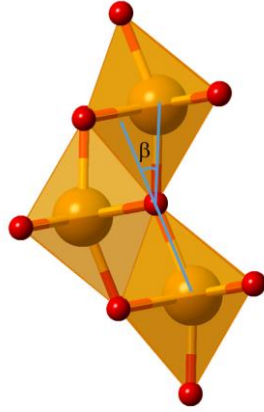
**Figure S20.** Fe-O-Fe path with 23 degree (β) tilt in γ–FeOOH
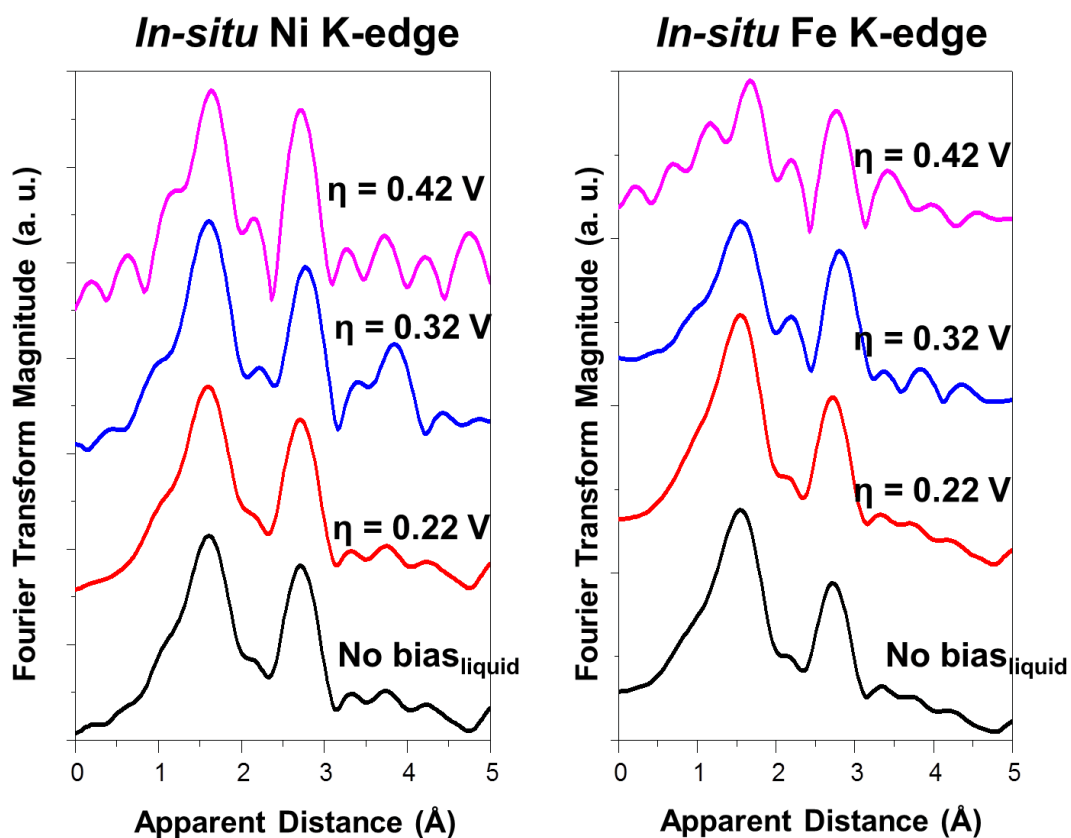
**Figure S21.** Fe and Ni K-edge EXAFS spectra (R-space) measured under operando conditions for the NiFe LDH sample. A large background ($\eta = 0.42$ V) present below 1 Å is due to the interference caused by generating gas bubbles.
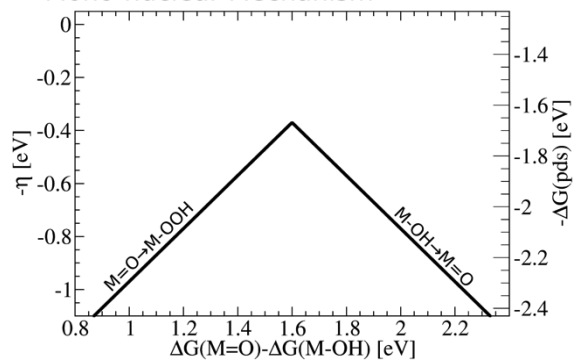
**Figure S22.** Volcano Plots. (a) Mono-nuclear mechanism. (b) Bi-functional mechanism.
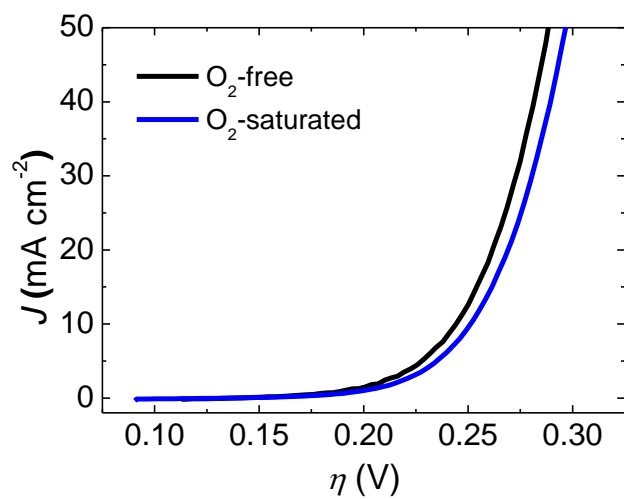
**Figure S23.** LSV curves conducted in $O_2$-saturated and $O_2$-free solutions.
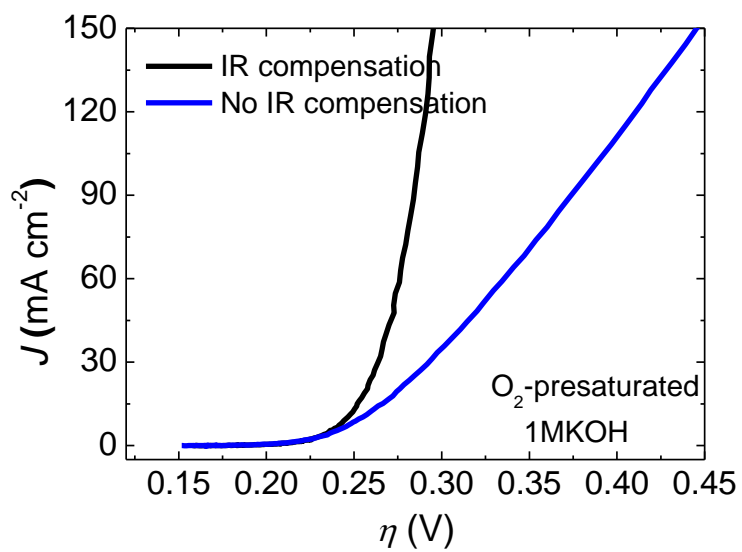
**Figure S24.** LSV curves in $O_2$ pre-saturated 1M KOH with and without iR compensation.

**Table S1.** Current densities and TOFs of all NF-AC-NiO$_x$-Fe electrodes (loading range: 0.96-14.07 μg cm$^{-2}$) at overpotentials of 250, 270, and 300 mV, respectively.

| NF-AC-NiO$_x$-Fe | Loading (μg cm$^{-2}$) | $\eta$@10 mA cm$^{-2}$ (mV) | J (mA cm$^{-2}$) [a] | | | | | | | | | TOF (s$^{-1}$) [b] | | |
| | | | 250 mV | | | 270 mV | | | 300 mV | | | 250 mV | 270 mV | 300 mV |
| | | | i | ii | iii | i | ii | iii | i | ii | iii | | | |
|---|---|---|---|---|---|---|---|---|---|---|---|---|---|---|
| 1# | 0.96 | 270 | 3.1 | 4.2 | / | 7.3 | 9.8 | / | 43 | 35 | / | 0.78±0.12 | 1.84±0.27 | 8.40±0.86 |
| 2# | 1.46 | 270 | 3.4 | 3.2 | / | 10.1 | 9.5 | / | 37 | 35 | / | 0.47±0.02 | 1.40±0.04 | 5.14±0.14 |
| 3# | 2.11 | 264 | 1.7 | 2.2 | / | 7.0 | 8.5 | / | 41.3 | 44.4 | / | 0.19±0.04 | 0.76±0.07 | 4.21±0.15 |
| 4# | 2.87 | 264 | 4.5 | 4.2 | / | 15.0 | 14.1 | / | 71.0 | 64.0 | / | 0.31±0.02 | 1.05±0.03 | 4.87±0.25 |
| 5# | 5.84 | 255 | 7.1 | 7.2 | 7.4 | 24.1 | 22.8 | 23 | 104 | 103 | 97.7 | 0.26±0.01 | 0.83±0.01 | 3.60±0.07 |
| 6# | 5.89 | 257 | 5.6 | 5.2 | 6.2 | 20.5 | 20.1 | 21.6 | 88.3 | 86.5 | 93 | 0.20±0.02 | 0.73±0.02 | 3.15±0.07 |
| 7# | 7.93 | 256 | 6.3 | 6.1 | 6.1 | 20.2 | 20.0 | 20.9 | 88.0 | 87.0 | 90.9 | 0.16±0.01 | 0.53±0.01 | 2.32±0.03 |
| 8# | 8.80 | 251 | 8.1 | 8.2 | 8.3 | 26.7 | 27.8 | 27.6 | 108 | 113 | 112 | 0.19±0.01 | 0.64±0.01 | 2.62±0.04 |
| 9# | 10.16 | 254 | 9.8 | 8.4 | 10 | 31.6 | 27.4 | 31.0 | 124 | 107 | 122 | 0.19±0.02 | 0.61±0.03 | 2.40±0.11 |
| 10# | 10.22 | 250 | 8.5 | 7.4 | 7.6 | 28.3 | 24.4 | 26.9 | 127 | 112 | 121 | 0.16±0.01 | 0.54±0.02 | 2.43±0.09 |
| 11# | 14.07 | 245 | 12.0 | 11.8 | 13.3 | 41.4 | 42.6 | 43.5 | 183 | 187 | 192 | 0.18±0.01 | 0.63±0.01 | 2.76±0.04 |

[a] Each sample is measured 2-3 times and the current densities for each measurement are listed (i, ii, and iii). [b] TOFs are based on the average current density for each sample. The error represents the standard error of results from 2-3 times' measurements. Except at the lowest loading, i.e, 1.0 μg cm$^{-2}$, the TOFs of samples with different loadings in this range are similar. The TOFs at 1.0 μg cm$^{-2}$ are significantly higher, in agreement with recent observations that at an ultralow loading ($\leq$ 1 μg cm$^{-2}$) the TOFs of certain OER catalysts were abnormally high compared to the same catalysts at loadings between 1.4 to 14.1 μg cm$^{-2}$. A "substrate effect"[7] or "nucleus sintering"[8] was invoked to rationalize these observations. The intrinsic activity, however, is best represented by TOFs at higher loadings[8]

**Table S2.** Current densities and TOFs of all Au-NiO$_x$-Fe electrodes (loading range: 0.98-2.13 µg cm$^{-2}$) at overpotentials of 250, 270, and 300 mV, respectively.

| Au-NiO$_x$-Fe | Loading (µg cm$^{-2}$) | $\eta$@10 mA cm$^{-2}$ (mV) | J (mA cm$^{-2}$) $^a$ | | | | | | TOF (s$^{-1}$) $^b$ | | |
|---|---|---|---|---|---|---|---|---|---|---|---|
| | | | 250 mV | | 270 mV | | 300 mV | | 250 mV | 270 mV | 300 mV |
| | | | i | ii | i | ii | i | ii | | | |
| 1# | 0.98 | 285 | 1.2 | 0.95 | 4.3 | 3.6 | 20 | 16 | 0.23±0.03 | 0.84±0.07 | 3.82±0.42 |
| 2# | 1.04 | 282 | 1.4 | 1.5 | 5.7 | 6.3 | 28.4 | 33.5 | 0.29±0.01 | 1.19±0.06 | 6.14±0.51 |
| 3# | 1.29 | 290 | 0.83 | 1.14 | 3.2 | 3.8 | 15 | 18 | 0.16±0.02 | 0.56±0.05 | 2.66±0.24 |
| 4# | 1.55 | 283 | 1.4 | 1.5 | 5.05 | 5.9 | 24 | 29.5 | 0.19±0.01 | 0.73±0.06 | 3.57±0.37 |
| 5# | 1.69 | 283 | 1.2 | 1.7 | 4.85 | 5.5 | 23.1 | 28 | 0.18±0.03 | 0.63±0.04 | 3.13±0.30 |
| 6# | 2.09 | 280 | 1.7 | 1.2 | 6 | 4.2 | 25.4 | 18.5 | 0.14±0.02 | 0.51±0.09 | 2.18±0.34 |
| 7# | 2.13 | 275 | 2.1 | 1.6 | 8.2 | 5.9 | 37 | 31 | 0.18±0.02 | 0.69±0.11 | 3.31±0.29 |

$^a$ Each sample is measured 2 times and the current densities for each measurement are listed (i and ii). $^b$ TOFs are based on the average current density for each sample. The error represents the standard error of results.

**Table S3.** Current densities and TOFs of all GC-NiO$_x$-Fe electrodes (loading range: 0.67-1.51 μg cm$^{-2}$) at overpotentials of 250, 270, and 300 mV, respectively.

| GC-NiO$_x$-Fe | Loading (μg cm$^{-2}$) | $\eta$@10 mA cm$^{-2}$ (mV) | $J$ (mA cm$^{-2}$) [a] | | | | | | TOF (s$^{-1}$) [b] | | |
|---|---|---|---|---|---|---|---|---|---|---|---|
| | | | 250 mV | | 270 mV | | 300 mV | | 250 mV | 270 mV | 300 mV |
| | | | i | ii | i | ii | i | ii | | | |
| 1# | 0.67 | 309 | 0.362 | 0.372 | 1.162 | 1.32 | 6.4 | 6.6 | 0.12±0.01 | 0.39±0.02 | 2.02±0.03 |
| 2# | 0.80 | 304 | 0.458 | 0.372 | 1.64 | 1.402 | 8.94 | 8 | 0.11±0.01 | 0.40±0.03 | 2.20±0.12 |
| 3# | 1.51 | 287 | 0.9066 | 0.94 | 3.6 | 3.78 | 21.2 | 22 | 0.13±0.01 | 0.51±0.01 | 2.96±0.05 |
| 4# | 2.11 | 277 | 1.91 | 1.55 | 7.23 | 5.66 | 30.1 | 25.0 | 0.16±0.02 | 0.60±0.10 | 2.75±0.33 |

[a] Each sample is measured 2 times and the current densities for each measurement are listed (i and ii). [b] TOFs are based on the average current density for each sample. The error represents the standard error of results.

**Table S4.** Current densities and TOFs of all NF–NiFeO$_x$ and GC-NiFeO$_x$ electrodes (loading range: 1.75-17.30 μg cm$^{-2}$) at overpotentials of 250, 270, and 300 mV, respectively.

| NiFeO$_x$ | | Loading (μg cm$^{-2}$) | $\eta$@10 mA cm$^{-2}$ (mV) | J (mA cm$^{-2}$) [a] | | | | | | TOF (s$^{-1}$) [b] | | |
|---|---|---|---|---|---|---|---|---|---|---|---|---|
| | | | | 250 mV | | 270 mV | | 300 mV | | 250 mV | 270 mV | 300 mV |
| | | | | i | ii | i | ii | i | ii | | | |
| NF | 1# | 1.97 | 338 | 0.224 | 0.235 | 0.65 | 0.697 | 3.04 | 2.73 | 0.023±0.003 | 0.062±0.011 | 0.409±0.072 |
| | 2# | 5.19 | 321 | 0.324 | 0.321 | 1.08 | 1.256 | 4.59 | 5.08 | 0.020±0.001 | 0.086±0.012 | 0.348±0.034 |
| | 3# | 5.54 | 321 | 0.325 | 0.352 | 0.866 | 1.00 | 3.94 | 4.20 | 0.020±0.002 | 0.050±0.009 | 0.264±0.017 |
| | 4# | 12.92 | 323 | 0.501 | 0.897 | 1.02 | 1.6 | 3.76 | 4.65 | 0.028±0.011 | 0.042±0.016 | 0.302±0.024 |
| GC | 5# | 1.75 | 360 | 0.048 | 0.057 | 0.128 | 0.16 | 0.736 | 0.894 | 0.027±0.002 | 0.075±0.008 | 0.424±0.041 |
| | 6# | 7.16 | 316 | 0.23 | 0.32 | 0.8 | 1.08 | 4.514 | 5.38 | 0.027±0.004 | 0.093±0.014 | 0.489±0.043 |
| | 7# | 11.97 | 308 | 0.558 | 0.67 | 1.94 | 2.22 | 7.8 | 8.12 | 0.036±0.003 | 0.122±0.008 | 0.465±0.009 |
| | 8# | 17.30 | 304 | 0.766 | 0.98 | 2.516 | 2.888 | 8.88 | 9.22 | 0.036±0.004 | 0.111±0.008 | 0.372±0.007 |

[a] Each sample is measured 2 times and the current densities for each measurement are listed (i and ii). [b] TOFs are based on the average current density for each sample. The error represents the standard error of results.

**Table S5.** Comparison of TOFs of different OER catalysts in thin film configurations (loading < 20 μg cm$^{-2}$) in alkaline solutions.

| Catalysts | TOF (s$^{-1}$) [a] | | | Reference |
|---|---|---|---|---|
| | 250 mV | 270 mV | 300 mV | |
| NF-AC-NiO$_x$-Fe | 0.24±0.10 | 0.78±0.27 | 3.35±1.06 | This work |
| Au-NiOx-Fe | 0.20±0.05 | 0.73±0.23 | 3.51±1.30 | This work |
| GC-NiOx-Fe | 0.13±0.02 | 0.48±0.10 | 2.48±0.44 | This work |
| NF-NiFeO$_x$ | 0.023±0.004 | 0.06±0.02 | 0.33±0.06 | This work |
| GC-NiFeO$_x$ | 0.032±0.005 | 0.10±0.02 | 0.44±0.05 | This work |
| NiFeO$_x$ | 0.02±0.004[d] | 0.072±0.02[d] | 0.52±0.16 | [24] |
| FeNiO$_x$ | 0.004±0.003 | 0.013±0.011 | 0.11±0.09 | [8] |
| CoFeO$_x$ | 0.011±0.001 | 0.047±0.003 | 0.31±0.02 | [8] |
| Ni$_{0.75}$Co$_{0.25}$O$_x$ | / | / | 0.089±0.013 | [25] |
| FeO$_x$ | / | / | 0.0015±0.0009 | [25] |
| NiO$_x$ [e] | / | / | 0.17±0.04 | [25] |
| CoO$_x$ | / | / | 0.0032±0.0014 | [25] |
| MnO$_x$ | / | / | 0.0004±0.0002 | [25] |
| IrO$_2$ | ~0.001[d] | ~0.002[d] | 0.0089±0.005 | [25] |

[a] For multiple samples, the averaged values with standard deviations are given for TOF. For NF-AC-NiO$_x$-Fe, Au-NiO$_x$-Fe, GC-NiO$_x$-Fe, NF-NiFeO$_x$, and GC-NiFeO$_x$, each sample is measured 2-3 times and the raw data are shown in Table S1-S4. For all iron-containing samples, iron is assumed as the active species. For samples without iron, all the other metal elements are assumed as the active species. The current densities are high and partially limited by mass-transport at η ≥ 300 mV, as reflected in the Tafel plots (Figure S3). Thus, the apparent TOFs of NF-AC-NiO$_x$-Fe at η ≥ 300 mV underestimate its intrinsic activity, and the TOFs at η = 250 and 270 mV are better representatives of the activity of this catalyst. [d] TOFs at these potentials were extrapolated using the reported Tafel slopes (~35 mV dec$^{-1}$ for NiFeO$_x$ and ~40 mV dec$^{-1}$ for IrO$_2$). [e] NiO$_x$ was likely to contain some Fe incorporated from electrolyte during the OER test.

**Table S6.** Comparison of TOFs of $NiFeO_x$ and NiFe LDH based OER catalysts in alkaline solutions from different groups.

| Catalysts | TOF ($s^{-1}$) [a] | | | Reference |
|---|---|---|---|---|
| | 250 mV | 270 mV | 300 mV | |
| NF-AC-NiO$_x$-Fe | 0.24±0.10 | 0.78±0.27 | 3.35±1.06 | This work |
| Au-NiOx-Fe | 0.20±0.05 | 0.73±0.23 | 3.51±1.30 | This work |
| GC-NiOx-Fe | 0.13±0.02 | 0.48±0.10 | 2.48±0.44 | This work |
| NF-NiFeO$_x$ | 0.023±0.004 | 0.06±0.02 | 0.33±0.06 | This work |
| GC-NiFeO$_x$ | 0.032±0.005 | 0.10±0.02 | 0.44±0.05 | This work |
| NiFeO$_x$ | 0.02±0.004[d] | 0.072±0.02[d] | 0.52±0.16 | [24, 26]Shannon W. Boettcher |
| NiFeO$_x$ | / | / | ~0.50 | [21]Alexis T. Bell |
| NiFeO$_x$ | / | / | ~0.45 | [5]Thomas F. Jaramillo |
| Ni$_{0.45}$Fe$_{0.55}$O$_x$ | / | / | ~0.28 | [27]Holger Dau and Peter Strasser |
| Fe(PO3)2/Ni2P | / | / | ~0.12 | [28]Zhifeng Ren |
| FeNiO$_x$ | / | / | ~0.11 | [29]Our group |
| Molecular NiFeO$_x$ | / | / | ~0.05 | [30]Xin Wang |
| NiFeO$_x$ | / | / | <0.08 | [31]Chuan Zhao |
| NiFe LDH nanosheets | / | / | ~0.15 | [32]Our group |
| NiFe LDH | / | / | ~0.12 | [33]Peter Strasser |
| NiFe@Graphene | / | / | ~0.1 | [34]Xinhe Bao |
| NiFe LDH | / | / | ~0.08 | [35]Harry B. Gray & Astrid M. Müller |
| NiFe LDH | / | / | ~0.06 | [36]Tierui Zhang |
| NiFe LDH | / | / | ~0.04 | [15, 37]Xue Duan |

**Table S7.** Specific current density ($J_s$) (normalized to the electrochemical surface area) at overpotentials of 250, 270, and 300 mV, respectively.

| Samples | $J_s$ (mA cm$^{-2}$) [a] | | | reference |
|---|---|---|---|---|
| | **250 mV** | **270 mV** | **300 mV** | |
| NF-AC-NiO$_x$-Fe | 0.013±0.005 | 0.041±0.018 | 0.18±0.08 | This work |
| NF-AC-FD-NiO$_x$-Fe | 0.019±0.002 | 0.051±0.008 | / | This work |
| NF -NiFeO$_x$ | 0.004±0.002 | 0.012±0.002 | 0.05±0.01 | This work |
| GC-NiO$_x$-Fe | 0.026±0.007 | 0.10±0.03 | 0.54±0.09 | This work |
| GC-NiFeO$_x$ | 0.008±0.003 | 0.03±0.01 | 0.13±0.04 | This work |
| NiFeO$_x$ [b] | 0.003 [c] | 0.011 [c] | 0.084 | [4] |
| NiFeO$_x$ [b] | 0.004±0.003 [c] | 0.015±0.010 [c] | 0.11±0.07 [c] | [6] |

[a] $J_s$ are based on the average $J_s$ for all samples of the same kind. The error represents the standard deviation of results. [b] The calculation of $J_s$ from the literature is shown in Supplementary Methods. [c] $J_s$ at these potentials are extrapolated using the reported Tafel slopes (~35 mV dec$^{-1}$)

**Table S8.** Comparison of η@10 mA cm$^{-2}$ of different OER catalysts in thin film configurations (loading < 20 μg cm$^{-2}$) alkaline solutions.

| Catalysts | Loading [b] (μg cm$^{-2}$) | η@10 mA cm$^{-2}$ (mV) | Reference |
|---|---|---|---|
| NF-AC-NiO$_x$-Fe [a] | 1.4-14.1 | 245-270 | This work |
| Au-NiOx-Fe [a] | 0.98-2.13 | 275-290 | This work |
| GC-NiOx-Fe [a] | 0.67-2.11 | 277-309 | This work |
| NF-NiFeO$_x$ [a] | 2.0-12.9 | 321-338 | This work |
| GC-NiFeO$_x$ [a] | 1.75-17.30 | 304-360 | This work |
| NiFeO$_x$ [a] | 1.2-12 | ~311 [c] | [24] |
| FeNiO$_x$ [a] | 1.3-3.0 | 370-378 | [8] |
| CoFeO$_x$ [a] | 1.9-5.5 | 333-349 | [8] |
| Ni$_{0.75}$Co$_{0.25}$O$_x$ | 1.04±0.09 | 445±2 | [25] |
| FeO$_x$ | 1.63±0.08 | 456±7 | [25] |
| NiO$_x$ [d] | 1.13±0.10 | 329±3 | [25] |
| CoO$_x$ | 1.32±0.14 | 423±13 | [25] |
| MnO$_x$ | 1.13±0.08 | 563±25 | [25] |
| IrO$_2$ | 4.12±0.14 | 427±5 | [25] |

[a] For multiple samples, the value ranges are given for loading and η@10mA cm$^{-2}$. For NF-AC-NiO$_x$-Fe, Au-NiO$_x$-Fe, GC-NiO$_x$-Fe, NF-NiFeO$_x$, and GC-NiFeO$_x$, the raw data are shown in Table S1-S4. [b] The loading is based on the quantity of the active metal species, in the form of metal oxides. [c] Overpotential is for the catalyst at the loading of around 8.3 ug cm$^{-2}$. [d] NiO$_x$ is likely to contain some Fe that were incorporated from electrolyte in the OER test.

**Table S9.** Comparison of the geometric activity of porous electrodes coated by a high-loading of catalysts in 1M KOH.

| Catalysts | Electrodes [a] | Loading (mg cm$^{-2}$) | $\eta$@10 mA cm$^{-2}$ (mV) | $\eta$@100 mA cm$^{-2}$ (mV) | Reference |
|---|---|---|---|---|---|
| NF-AC-FD-NiO$_x$-Fe | NF | 0.068 | 215 | 248 | This work |
| Fe(PO$_3$)$_2$/Ni$_2$P | NF | 8.0 [b] | 177 [c] | 221 | 28 |
| G-FeCoW | NF(Au coated) | 0.4 | 191±3 | / | 14 |
| Ni$_2$P-Ni | NF | / | 200 | 268 | 38 |
| EG/Co$_{0.85}$Se/NiFe LDH | Graphene Foam | 4.0 | 203 | 260 | 39 |
| Ni$_{60}$Fe$_{30}$Mn$_{10}$ | Alloy Foam | 76. 0 | 208 | 270 | 40 |
| NiFeO$_x$ | CFP | 1.6 | 230 | 271 | 41 |
| NiFe hydroxides | NF | / | 245 | 280 | 42 |
| NiSe | NF | 2.8 | 251 | 314 | 43 |
| NiFe LDH | NF | 1.0 | 240-256 | ~306 | 44, 45 |
| IrO$_2$ | CFP | 3.3 | 264 | / | 46, 47 |

[a] NF: nickel foam; CFP: carbon fiber paper. [b] Loading of Fe(PO$_3$)$_2$. [c] Overpotential at this current density was extrapolated using the reported Tafel slopes (~52 mV dec$^{-1}$).

**Table S10.** Structural parameters of γ–FeOOH, NiFe LDH and NF-AC-NiO$_x$-Fe samples extracted from EXAFS refinement.

| path | R (Å) | CN | ΔE (eV) | σ² (Å²) | R-value (%) |
|---|---|---|---|---|---|
| **γ-FeOOH** | | | | | |
| **Fe-O** | 1.99(4) | 6.4(3) | -5.9(3) | 0.0088(5) | 2.035 |
| **Fe-Fe** | 3.08(6) | 5.4(5) | -4.3(7) | 0.0082(4) | |
| **NiFe LDH** | | | | | |
| **Fe-O** | 2.00(1) | 5.8(1) | -5.0(6) | 0.0071(1) | 1.429 |
| **Fe-Fe** | 3.07(1) | 3.4(3) | -1.1(9) | 0.0085(3) | |
| **Fe-Ni$_{Oh}$** | 3.11(2) | 2.6(4) | -7.9(8) | 0.0055(4) | |
| **NF-AC-NiOx-Fe** | | | | | |
| **Fe-O** | 1.98(1) | 4.8(2) | 0.1(8) | 0.0090(2) | 7.801 |
| **Fe-Fe(Ni)** | 3.10(2) | 5.0(2) | 1.8(6) | 0.0115(1) | |
| **Fe-Ni$_{outside}$** | 3.98(4) | 3.8(4) | 0.6(7) | 0.0051(6) | |

**Table S11.** Structural parameters of Au-NiO$_x$-Fe sample extracted from Ni K-edge EXAFS measured under ex situ and operando conditions.

| condition | path | R (Å) | CN | ΔE (eV) | σ² (Å²) | R-value (%) |
|---|---|---|---|---|---|---|
| **Dry sample** | **Ni-O** | 2.04(4) | 6.0(3) | -5.1(5) | 0.0076(4) | 2.517 |
| | **Ni-Ni** | 3.09(5) | 6.1(1) | -1.0(6) | 0.0076(3) | |
| **No bias** | **Ni-O** | 2.04(4) | 6.0(3) | -5.4(5) | 0.0081(9) | 2.023 |
| | **Ni-Ni** | 3.10(6) | 6.1(6) | 1.5(7) | 0.0071(9) | |
| **η = 0.22** | **Ni-O** | 2.04(3) | 6.0(1) | -5.6(5) | 0.0072(9) | 2.386 |
| | **Ni-Ni** | 3.10(5) | 6.0(2) | -5.7(7) | 0.0068(9) | |
| **η = 0.27** | **Ni-O** | 1.86(4) | 5.5(1) | -7.2(5) | 0.0080(1) | 3.170 |
| | **Ni-Ni** | 2.82(6) | 5.1(4) | -2.3(9) | 0.0076(1) | |
| **η = 0.32** | **Ni-O** | 1.88(4) | 5.6(2) | -4.9(3) | 0.0080(1) | 3.209 |
| | **Ni-Ni** | 2.84(4) | 5.0(3) | -3.9(6) | 0.0064(1) | |
| **η = 0.37** | **Ni-O** | 1.89(2) | 5.6(2) | -3.6(4) | 0.0059(3) | 6.667 |
| | **Ni-Ni** | 2.85(3) | 5.0(3) | 1.8(6) | 0.0058(2) | |

**Table S12.** CNs of Fe-Fe(Ni) path (path A) and Fe-Ni$_{outside}$ path (path B) for the structure models of Figure S15.

| | Surface | | Step I | | Step II | |
|---|---|---|---|---|---|---|
| | CN$_{path A}$ | CN$_{path B}$ | CN$_{path A}$ | CN$_{path B}$ | CN$_{path A}$ | CN$_{path B}$ |
| Before OER | **4-5** | 3 | **6-7** | 3 | **7-8** | 5 |
| Under OER (No tilt) | **4-5** | 3 | **4-5** | 3 | **4-5** | 3 |
| Under OER (Tilt) | 2-3 | ~2 | 2-3 | ~2 | 2-3 | ~2 |

# References

(1) de Faria, D. L. A.; Venâncio Silva, S.; de Oliveira, M. T. Raman microspectroscopy of some iron oxides and oxyhydroxides. *J. Raman Spectrosc.* **1997,** *28*, 873-878.

(2) Yeo, B. S.; Bell, A. T. In situ Raman study of nickel oxide and gold-supported nickel oxide catalysts for the electrochemical evolution of oxygen. *J. Phys. Chem. C* **2012,** *116*, 8394-8400.

(3) Gregoire, B.; Ruby, C.; Carteret, C. Hydrolysis of mixed $Ni^{2+}$-$Fe^{3+}$ and $Mg^{2+}$-$Fe^{3+}$ solutions and mechanism of formation of layered double hydroxides. *Dalton Trans.* **2013,** *42*, 15687-15698.

(4) Batchellor, A. S.; Boettcher, S. W. Pulse-electrodeposited Ni-Fe (oxy)hydroxide oxygen evolution electrocatalysts with high geometric and intrinsic activities at large mass loadings. *ACS Catal.* **2015,** *5*, 6680-6689.

(5) Chakthranont, P.; Kibsgaard, J.; Gallo, A.; Park, J.; Mitani, M.; Sokaras, D.; Kroll, T.; Sinclair, R.; Mogensen, M. B.; Jaramillo, T. F. Effects of gold substrates on the intrinsic and extrinsic activity of high-loading nickel-based oxyhydroxide oxygen evolution catalysts. *ACS Catal.* **2017,** *7*, 5399-5409.

(6) McCrory, C. C. L.; Jung, S. H.; Peters, J. C.; Jaramillo, T. F. Benchmarking heterogeneous electrocatalysts for the oxygen evolution reaction. *J. Am. Chem. Soc.* **2013,** *135*, 16977-16987.

(7) Yeo, B. S.; Bell, A. T. Enhanced activity of gold-supported cobalt oxide for the electrochemical evolution of oxygen. *J. Am. Chem. Soc.* **2011,** *133*, 5587-5593.

(8) Morales-Guio, C. G.; Liardet, L.; Hu, X. Oxidatively electrodeposited thin-film transition metal (oxy)hydroxides as oxygen evolution catalysts. *J. Am. Chem. Soc.* **2016,** *138*, 8946-8957.

(9) Vantelon, D.; Trcera, N.; Roy, D.; Moreno, T.; Mailly, D.; Guilet, S.; Metchalkov, E.; Delmotte, F.; Lassalle, B.; Lagarde, P.; Flank, A.-M. The LUCIA beamline at SOLEIL. *J. Synchrotron Radiat.* **2016,** *23*, 635-640.

(10) Rehr, J. J.; Albers, R. C. Theoretical approaches to X-ray absorption fine structure. *Rev. Mod. Phys.* **2000,** *72*, 621-654.

(11) Newville, M. EXAS analysis using FEFF and FEFFIT. *J. Synchrotron Radiat.* **2001,** *8*, 96-100.

(12) Diaz-Morales, O.; Ledezma-Yanez, I.; Koper, M. T. M.; Calle-Vallejo, F. Guidelines for the rational design of Ni-based double hydroxide electrocatalysts for the oxygen evolution reaction. *ACS Catal.* **2015,** *5*, 5380-5387.

(13) Man, I. C.; Su, H. Y.; Calle-Vallejo, F.; Hansen, H. A.; Martinez, J. I.; Inoglu, N. G.; Kitchin, J.; Jaramillo, T. F.; Norskov, J. K.; Rossmeisl, J. Universality in oxygen evolution electrocatalysis on oxide surfaces. *ChemCatChem* **2011,** *3*, 1159-1165.

(14) Zhang, B.; Zheng, X. L.; Voznyy, O.; Comin, R.; Bajdich, M.; Garcia-Melchor, M.; Han, L. L.; Xu, J. X.; Liu, M.; Zheng, L. R.; de Arquer, F. P. G.; Dinh, C. T.; Fan, F. J.; Yuan, M. J.; Yassitepe, E.; Chen, N.; Regier, T.; Liu, P. F.; Li, Y. H.; De Luna, P.; Janmohamed, A.; Xin, H. L. L.; Yang, H. G.; Vojvodic, A.; Sargent, E. H. Homogeneously dispersed multimetal oxygen-evolving catalysts. *Science* **2016,** *352*, 333-337.

(15) Frydendal, R.; Busch, M.; Halck, N. B.; Paoli, E. A.; Krtil, P.; Chorkendorff, I.; Rossmeisl, J. Enhancing activity for the oxygen evolution reaction: The beneficial interaction of gold with manganese and cobalt oxides. *ChemCatChem* **2015,** *7*, 149-154.

(16) Bajdich, M.; Garcia-Mota, M.; Vojvodic, A.; Norskov, J. K.; Bell, A. T. Theoretical investigation of the activity of cobalt oxides for the electrochemical oxidation of water. *J. Am. Chem. Soc.* **2013,** *135*, 13521-13530.

(17) Hedenstedt, K.; Gomes, A. S. O.; Busch, M.; Ahlberg, E. Study of hypochlorite reduction related to the sodium chlorate process. *Electrocatalysis* **2016,** *7*, 326-335.

(18) Calle-Vallejo, F.; Krabbe, A.; García-Lastra, J. M. How covalence breaks adsorption-energy scaling relations and solvation restores them. *Chem. Sci.* **2017,** *8*, 124-130.

(19) Busch, M.; Fabrizio, A.; Luber, S.; Hutter, J.; Corminboeuf, C. Exploring the limitation of molecular water oxidation catalysts. *J. Phys. Chem. C* **2018,** *122*, 12404-12412.

(20) Yin, L. I.; Yellin, E.; Adler, I. X□ray excited LMM Auger spectra of copper, nickel, and iron. *J. Appl. Phys.* **1971,** *42*, 3595-3600.

(21) Louie, M. W.; Bell, A. T. An investigation of thin-film Ni–Fe oxide catalysts for the electrochemical evolution of oxygen. *J. Am. Chem. Soc.* **2013,** *135*, 12329-12337.

(22) Biesinger, M. C.; Payne, B. P.; Grosvenor, A. P.; Lau, L. W. M.; Gerson, A. R.; Smart, R. S. C. Resolving surface chemical states in xps analysis of first row transition metals, oxides and hydroxides: Cr, Mn, Fe, Co and Ni. *Appl. Surf. Sci.* **2011,** *257,* 2717-2730.

(23) Grosvenor, A. P.; Kobe, B. A.; Biesinger, M. C.; McIntyre, N. S. Investigation of multiplet splitting of Fe 2p XPS spectra and bonding in iron compounds. *Surf. Interface Anal.* **2004,** *36,* 1564-1574.

(24) Trotochaud, L.; Young, S. L.; Ranney, J. K.; Boettcher, S. W. Nickel-iron oxyhydroxide oxygen-evolution electrocatalysts: The role of intentional and incidental iron incorporation. *J. Am. Chem. Soc.* **2014,** *136,* 6744-6753.

(25) Trotochaud, L.; Ranney, J. K.; Williams, K. N.; Boettcher, S. W. Solution-cast metal oxide thin film electrocatalysts for oxygen evolution. *J. Am. Chem. Soc.* **2012,** *134,* 17253-17261.

(26) Stevens, M. B.; Enman, L. J.; Batchellor, A. S.; Cosby, M. R.; Vise, A. E.; Trang, C. D. M.; Boettcher, S. W. Measurement techniques for the study of thin film heterogeneous water oxidation electrocatalysts. *Chem. Mater.* **2017,** *29,* 120-140.

(27) Görlin, M.; Chernev, P.; Ferreira de Araújo, J.; Reier, T.; Dresp, S.; Paul, B.; Krähnert, R.; Dau, H.; Strasser, P. Oxygen evolution reaction dynamics, faradaic charge efficiency, and the active metal redox states of Ni–Fe oxide water splitting electrocatalysts. *J. Am. Chem. Soc.* **2016,** *138,* 5603-5614.

(28) Zhou, H. Q.; Yu, F.; Sun, J. Y.; He, R.; Chen, S.; Chu, C. W.; Ren, Z. F. Highly active catalyst derived from a 3d foam of $Fe(PO_3)_2/Ni_2P$ for extremely efficient water oxidation. *Proc. Natl. Acad. Sci. U. S. A.* **2017,** *114,* 5607-5611.

(29) Morales-Guio, C. G.; Liardet, L.; Hu, X. Oxidatively electrodeposited thin-film transition metal (oxy)hydroxides as oxygen evolution catalysts. *J. Am. Chem. Soc.* **2016,** *138,* 8946-8957.

(30) Wang, J.; Gan, L.; Zhang, W.; Peng, Y.; Yu, H.; Yan, Q.; Xia, X.; Wang, X. In situ formation of molecular Ni-Fe active sites on heteroatom-doped graphene as a heterogeneous electrocatalyst toward oxygen evolution. *Sci. Adv.* **2018,** *4,* eaap7970.

(31) Lu, X.; Zhao, C. Electrodeposition of hierarchically structured three-dimensional nickel–iron electrodes for efficient oxygen evolution at high current densities. *Nat. Commun.* **2015,** *6,* 6616.

(32) Song, F.; Hu, X. Exfoliation of layered double hydroxides for enhanced oxygen evolution catalysis. *Nat. Commun.* **2014,** *5,* 4477.

(33) Dionigi, F.; Reier, T.; Pawolek, Z.; Gliech, M.; Strasser, P. Design criteria, operating conditions, and nickel–iron hydroxide catalyst materials for selective seawater electrolysis. *ChemSusChem* **2016,** *9,* 962-972.

(34) Cui, X.; Ren, P.; Deng, D.; Deng, J.; Bao, X. Single layer graphene encapsulating non-precious metals as high-performance electrocatalysts for water oxidation. *Energy Environ. Sci.* **2016,** *9,* 123-129.

(35) Hunter, B. M.; Blakemore, J. D.; Deimund, M.; Gray, H. B.; Winkler, J. R.; Müller, A. M. Highly active mixed-metal nanosheet water oxidation catalysts made by pulsed-laser ablation in liquids. *J. Am. Chem. Soc.* **2014,** *136,* 13118-13121.

(36) Zhao, Y.; Zhang, X.; Jia, X.; Waterhouse, G. I. N.; Shi, R.; Zhang, X.; Zhan, F.; Tao, Y.; Wu, L.-Z.; Tung, C.-H.; O'Hare, D.; Zhang, T. Sub-3 nm ultrafine monolayer layered double hydroxide nanosheets for electrochemical water oxidation. *Adv. Energy Mater.* **2018,** *8,* 1703585.

(37) Lu, Z.; Xu, W.; Zhu, W.; Yang, Q.; Lei, X.; Liu, J.; Li, Y.; Sun, X.; Duan, X. Three-dimensional NiFe layered double hydroxide film for high-efficiency oxygen evolution reaction. *Chem. Commun.* **2014,** *50,* 6479-6482.

(38) You, B.; Jiang, N.; Sheng, M. L.; Bhushan, M. W.; Sun, Y. J. Hierarchically porous urchin-like $Ni_2P$ superstructures supported on nickel foam as efficient bifunctional electrocatalysts for overall water splitting. *ACS Catal.* **2016,** *6,* 714-721.

(39) Hou, Y.; Lohe, M. R.; Zhang, J.; Liu, S.; Zhuang, X.; Feng, X. Vertically oriented cobalt selenide/NiFe layered-double-hydroxide nanosheets supported on exfoliated graphene foil: An efficient 3d electrode for overall water splitting. *Energy Environ. Sci.* **2016,** *9,* 478-483.

(40) Detsi, E.; Cook, J. B.; Lesel, B. K.; Turner, C. L.; Liang, Y. L.; Robbennolt, S.; Tolbert, S. H. Mesoporous $Ni_{60}Fe_{30}Mn_{10}$-alloy based metal/metal oxide composite thick films as highly active and robust oxygen evolution catalysts. *Energy Environ. Sci.* **2016,** *9,* 540-549.

(41) Wang, H. T.; Lee, H. W.; Deng, Y.; Lu, Z. Y.; Hsu, P. C.; Liu, Y. Y.; Lin, D. C.; Cui, Y. Bifunctional non-noble metal oxide nanoparticle electrocatalysts through lithium-induced conversion for overall water splitting. *Nat. Commun.* **2015,** *6,* 7261.

(42) Lu, X. Y.; Zhao, C. A. Electrodeposition of hierarchically structured three-dimensional nickel-iron electrodes for efficient oxygen evolution at high current densities. *Nat. Commun.* **2015,** *6,* 6616.

(43) Tang, C.; Cheng, N.; Pu, Z.; Xing, W.; Sun, X. NiSe nanowire film supported on nickel foam: An efficient and stable 3d bifunctional electrode for full water splitting. *Angew. Chem. Int. Ed.* **2015,** *54*, 9351-9355.

(44) Lu, Z.; Xu, W. W.; Zhu, W.; Yang, Q.; Lei, X. D.; Liu, J. F.; Li, Y. P.; Sun, X. M.; Duan, X. Three-dimensional NiFe layered double hydroxide film for high-efficiency oxygen evolution reaction. *Chem. Commun.* **2014,** *50*, 6479-6482.

(45) Luo, J. S.; Im, J. H.; Mayer, M. T.; Schreier, M.; Nazeeruddin, M. K.; Park, N. G.; Tilley, S. D.; Fan, H. J.; Gratzel, M. Water photolysis at 12.3% efficiency via perovskite photovoltaics and earth-abundant catalysts. *Science* **2014,** *345*, 1593-1596.

(46) Yan, X. D.; Li, K. X.; Lyu, L.; Song, F.; He, J.; Niu, D. M.; Liu, L.; Hu, X. L.; Chen, X. B. From water oxidation to reduction: Transformation from $Ni_xCo_{3-x}O_4$ nanowires to $NiCo/NiCoO_x$ heterostructures. *ACS Appl. Mater. Interfaces* **2016,** *8*, 3208-3214.

(47) Wang, P.; Song, F.; Amal, R.; Ng, Y. H.; Hu, X. Efficient water splitting catalyzed by cobalt phosphide-based nanoneedle arrays supported on carbon cloth. *ChemSusChem* **2016,** *9*, 472-477.

# DFT Structures

γ-FeOOH (010) – Fe bare

Cell:

25.000000000000000   0.000000000000000   0.000000000000000   -
3.1524999999999999   5.4602851999999995   0.000000000000000
0.000000000000000   -0.000000000000000   10.000000000000000

xyz coordinates

| | | | |
|---|---|---|---|
| O | 5.67344417 | 1.30902184 | 3.94323191 |
| O | 4.09719417 | 4.03916444 | 3.94323191 |
| O | 8.82594417 | 1.30902184 | 3.94323191 |
| O | 7.24969417 | 4.03916444 | 3.94323191 |
| O | 11.97844417 | 1.30902184 | 3.94323191 |
| O | 10.40219417 | 4.03916444 | 3.94323191 |
| O | 15.17307106 | 1.45864325 | 3.91920680 |
| O | 13.68149577 | 4.00907130 | 3.92803847 |
| O | 17.81995030 | 1.09068833 | 3.65023839 |
| O | 7.25610552 | 2.21574101 | 6.00454361 |
| O | 5.67985552 | 4.94588361 | 6.00454361 |
| O | 10.40860552 | 2.21574101 | 6.00454361 |
| O | 8.83235552 | 4.94588361 | 6.00454361 |
| O | 13.50860992 | 2.18274513 | 6.06554899 |
| O | 12.07800776 | 5.00972327 | 5.82538241 |
| O | 16.67367052 | 2.14796858 | 6.04065515 |
| O | 15.12133226 | 4.91031827 | 5.92254901 |
| Fe | 7.25384250 | 0.39563374 | 5.12304955 |
| Fe | 5.67759250 | 3.12577634 | 5.12304955 |
| Fe | 10.40634250 | 0.39563374 | 5.12304955 |
| Fe | 8.83009250 | 3.12577634 | 5.12304955 |
| Fe | 13.53896568 | 0.36290398 | 5.20953084 |
| Fe | 11.94959123 | 3.14078623 | 5.21673059 |
| Fe | 16.78322813 | 0.44009994 | 4.79266526 |
| Fe | 15.05880971 | 3.05232639 | 5.31171158 |
| H | 8.83976609 | 1.30304303 | 2.96881635 |
| H | 7.26351609 | 4.03318563 | 2.96881635 |
| H | 11.99226609 | 1.30304303 | 2.96881635 |
| H | 10.41601609 | 4.03318563 | 2.96881635 |
| H | 15.39095324 | 1.65072463 | 2.99186186 |
| H | 13.93602091 | 4.06492206 | 2.99245410 |
| H | 15.37302592 | 5.17766082 | 6.82055985 |
| H | 16.60056161 | 1.92167597 | 6.98352733 |

γ-FeOOH (010) – Fe-OH

Cell:

25.000000000000000    0.000000000000000    0.000000000000000    -
3.152499999999999    5.460285199999995    0.000000000000000
0.000000000000000    -0.000000000000000    10.000000000000000

<u>xyz coordinates</u>

| | | | |
|---|---|---|---|
| O | 5.36816161 | 1.35136899 | 3.98052770 |
| O | 3.79191161 | 4.08151159 | 3.98052770 |
| O | 8.52066161 | 1.35136899 | 3.98052770 |
| O | 6.94441161 | 4.08151159 | 3.98052770 |
| O | 11.67316161 | 1.35136899 | 3.98052770 |
| O | 10.09691161 | 4.08151159 | 3.98052770 |
| O | 14.79150953 | 1.17044360 | 3.87039109 |
| O | 13.31166528 | 3.96332554 | 3.87024155 |
| O | 17.49656795 | 1.22171150 | 3.89884562 |
| O | 16.04124007 | 3.81833988 | 3.87285374 |
| O | 6.95082297 | 2.25808815 | 6.04183940 |
| O | 5.37457297 | 4.98823075 | 6.04183940 |
| O | 10.10332297 | 2.25808815 | 6.04183940 |
| O | 8.52707297 | 4.98823075 | 6.04183940 |
| O | 13.31527348 | 2.32200284 | 5.93071330 |
| O | 11.71003906 | 5.01383284 | 5.93156759 |
| O | 16.03107459 | 2.27346355 | 6.11453774 |
| O | 14.50480999 | 5.02744240 | 6.09527404 |
| Fe | 6.94855994 | 0.43798089 | 5.1603453 |
| Fe | 5.37230994 | 3.16812349 | 5.1603453 |
| Fe | 10.10105994 | 0.43798089 | 5.1603453 |
| Fe | 8.52480994 | 3.16812349 | 5.1603453 |
| Fe | 13.23350086 | 0.43476777 | 5.2140221 |
| Fe | 11.63805066 | 3.18048559 | 5.2271521 |
| Fe | 16.37250049 | 0.49849419 | 4.9153296 |
| Fe | 14.77403854 | 3.23388839 | 5.0281536 |
| H | 8.53448353 | 1.34539018 | 3.00611213 |
| H | 6.95823353 | 4.07553278 | 3.00611213 |
| H | 11.68698353 | 1.34539018 | 3.00611213 |
| H | 10.11073353 | 4.07553278 | 3.00611213 |
| H | 14.97960021 | 1.38450560 | 2.94210460 |
| H | 13.61900321 | 4.11913077 | 2.95994111 |
| H | 16.82518154 | 3.22270614 | 3.87908090 |
| H | 13.99741684 | 4.80382083 | 6.89819126 |
| H | 15.55266149 | 2.00536458 | 6.92258046 |

γ-FeOOH (010) – Fe=O

Cell:

25.000000000000000    0.000000000000000    0.000000000000000    -
3.1524999999999999    5.4602851999999995    0.000000000000000
0.000000000000000    -0.000000000000000    10.0000000000000000

<u>xyz coordinates</u>

| | | | |
|----|-----------|-----------|-----------|
| O  | 5.68684391  | 1.34165963 | 4.04134256 |
| O  | 4.11059391  | 4.07180223 | 4.04134256 |
| O  | 8.83934391  | 1.34165963 | 4.04134256 |
| O  | 7.26309391  | 4.07180223 | 4.04134256 |
| O  | 11.99184391 | 1.34165963 | 4.04134256 |
| O  | 10.41559391 | 4.07180223 | 4.04134256 |
| O  | 15.11709353 | 1.35754201 | 3.99105782 |
| O  | 13.53971957 | 4.09613414 | 3.98691172 |
| O  | 17.87330828 | 1.13586189 | 4.04405427 |
| O  | 16.30002307 | 3.85351788 | 4.04164799 |
| O  | 7.26950527  | 2.24837879 | 6.10265426 |
| O  | 5.69325527  | 4.97852139 | 6.10265426 |
| O  | 10.42200527 | 2.24837879 | 6.10265426 |
| O  | 8.84575527  | 4.97852139 | 6.10265426 |
| O  | 13.58199497 | 2.28692099 | 6.01894533 |
| O  | 12.00512062 | 5.01586984 | 6.01892834 |
| O  | 16.42589402 | 2.11463257 | 6.18913178 |
| O  | 14.83898906 | 4.85937360 | 6.18406665 |
| Fe | 7.26724224  | 0.42827153 | 5.2211602 |
| Fe | 5.69099224  | 3.15841413 | 5.2211602 |
| Fe | 10.41974224 | 0.42827153 | 5.2211602 |
| Fe | 8.84349224  | 3.15841413 | 5.2211602 |
| Fe | 13.55229131 | 0.44881578 | 5.3056220 |
| Fe | 11.97649848 | 3.17910472 | 5.3040863 |
| Fe | 16.72919895 | 0.47416677 | 5.0544928 |
| Fe | 15.15513982 | 3.20235933 | 5.0578390 |
| H  | 8.85316583  | 1.33568082 | 3.06692699 |
| H  | 7.27691583  | 4.06582342 | 3.06692699 |
| H  | 12.00566583 | 1.33568082 | 3.06692699 |
| H  | 10.42941583 | 4.06582342 | 3.06692699 |
| H  | 15.36286868 | 1.50413367 | 3.06163934 |
| H  | 13.79396391 | 4.23931386 | 3.05861229 |
| H  | 14.31486070 | 4.57540816 | 6.95842705 |
| H  | 15.90560465 | 1.82153153 | 6.96340730 |

γ-FeOOH (010) – Fe-OOH

Cell:

25.000000000000000    0.000000000000000    0.000000000000000    -
3.1524999999999999    5.4602851999999995    0.000000000000000
0.000000000000000    -0.000000000000000    10.000000000000000

<u>xyz coordinates</u>

| | | | |
|---|---|---|---|
| O | 4.97425609 | 1.34326757 | 4.04114476 |
| O | 3.39800609 | 4.07341017 | 4.04114476 |
| O | 8.12675609 | 1.34326757 | 4.04114476 |
| O | 6.55050609 | 4.07341017 | 4.04114476 |
| O | 11.27925609 | 1.34326757 | 4.04114476 |
| O | 9.70300609 | 4.07341017 | 4.04114476 |
| O | 14.37494270 | 1.31239559 | 3.95782111 |
| O | 12.88601822 | 4.08959427 | 3.95478847 |
| O | 17.13540627 | 1.25212825 | 4.02535647 |
| O | 15.67720214 | 3.93856184 | 3.98408227 |
| O | 6.55691744 | 2.24998673 | 6.10245646 |
| O | 4.98066744 | 4.98012933 | 6.10245646 |
| O | 9.70941744 | 2.24998673 | 6.10245646 |
| O | 8.13316744 | 4.98012933 | 6.10245646 |
| O | 12.87579835 | 2.31089178 | 6.01778529 |
| O | 11.31671405 | 5.03858553 | 5.97651478 |
| O | 15.68809582 | 2.15375160 | 6.22055239 |
| O | 14.13492143 | 4.94307047 | 6.21630742 |
| O | 17.01743116 | 3.83153828 | 4.29546924 |
| Fe | 6.55465441 | 0.42987947 | 5.2209624 |
| Fe | 4.97840441 | 3.16002207 | 5.2209624 |
| Fe | 9.70715441 | 0.42987947 | 5.2209624 |
| Fe | 8.13090441 | 3.16002207 | 5.2209624 |
| Fe | 12.82772607 | 0.45055589 | 5.2736390 |
| Fe | 11.24548236 | 3.18605996 | 5.2866508 |
| Fe | 15.98545165 | 0.49671911 | 5.0122754 |
| Fe | 14.40137119 | 3.22905970 | 5.1504895 |
| H | 8.14057801 | 1.33728876 | 3.06672919 |
| H | 6.56432801 | 4.06743136 | 3.06672919 |
| H | 11.29307801 | 1.33728876 | 3.06672919 |
| H | 9.71682801 | 4.06743136 | 3.06672919 |
| H | 14.55048860 | 1.45033766 | 3.01185629 |
| H | 13.11588939 | 4.21733248 | 3.01858501 |
| H | 13.64253510 | 4.69781545 | 7.02253764 |
| H | 15.23597810 | 1.83582836 | 7.02477490 |
| H | 17.20530071 | 2.82580563 | 4.15689959 |

γ-Ni(OH)₂ (0001) – reduced

Cell:

6.535012   0.0   0.0
-3.267506   5.6594901   0.0
0.0   0.0   12.0

xyz-coordinates

| | | | |
|----|----|----|----|
| O | 1.90311068 | 1.41387317 | 5.00563898 |
| H | 1.86929724 | 1.41709539 | 4.03660623 |
| Ni | 0.27517317 | 0.47174663 | 5.99909845 |
| O | 0.28113025 | 2.35770323 | 6.99385990 |
| H | 0.29466067 | 2.32533586 | 7.96317989 |
| O | 0.26935913 | 4.24361866 | 5.00563819 |
| H | 0.23554433 | 4.24683978 | 4.03660658 |
| Ni | -1.35857973 | 3.30148646 | 5.99909642 |
| O | -1.35262429 | 5.18744783 | 6.99386051 |
| H | -1.33909241 | 5.15508162 | 7.96317950 |
| O | 5.17061670 | 1.41387146 | 5.00563836 |
| H | 5.13680387 | 1.41709566 | 4.03660661 |
| Ni | 3.54267462 | 0.47174416 | 5.99910022 |
| O | 3.54863603 | 2.35770490 | 6.99386049 |
| H | 3.56216605 | 2.32533563 | 7.96317953 |
| O | 3.53686615 | 4.24361635 | 5.00563620 |
| H | 3.50305099 | 4.24684001 | 4.03660632 |
| Ni | 1.90892188 | 3.30148425 | 5.99909835 |
| O | 1.91488068 | 5.18745005 | 6.99386258 |
| H | 1.92841295 | 5.15508138 | 7.96317976 |

γ-Ni(OH)$_2$ (0001) – oxidised

Cell:

6.535012  0.0  0.0
-3.267506  5.6594901  0.0
0.0  0.0  12.0

xyz-coordinates

| | | | |
|---|---|---|---|
| O | 1.90718120 | 1.41024989 | 5.11026479 |
| Ni | 0.33748037 | 0.50393985 | 5.97035697 |
| O | 0.26348653 | 2.36150202 | 7.00954288 |
| H | 0.28606505 | 2.34548947 | 7.97964602 |
| O | 0.25860079 | 4.23283676 | 5.01888013 |
| H | 0.24039563 | 4.23769611 | 4.04831928 |
| Ni | -1.36355305 | 3.29546123 | 5.99983967 |
| O | -1.35787566 | 5.17103119 | 7.01106629 |
| H | -1.34931908 | 5.16992087 | 7.98178655 |
| O | 5.16590280 | 1.41902658 | 5.02110175 |
| H | 5.15659766 | 1.43180123 | 4.05041585 |
| Ni | 3.47666637 | 0.50131379 | 5.97375789 |
| O | 3.55851614 | 2.35766582 | 7.01412879 |
| H | 3.55697017 | 2.34679260 | 7.98470186 |
| O | 3.54206516 | 4.22879661 | 5.02092673 |
| H | 3.54183501 | 4.23319442 | 4.05010419 |
| Ni | 1.90588953 | 3.22201426 | 5.97196221 |
| O | 1.90368936 | 5.18413400 | 6.88979005 |
| H | 1.91840602 | 5.17262113 | 7.86117393 |

γ-NiOOH (0001) – reduced

Cell:

6.065992   0.0   0.0
-3.032996   5.2533066   0.0
0.0   0.0   12.0


xyz-coordinates

O     1.71076370      1.37210496      5.12338706
H     1.67051527      1.39634735      4.15397780
Ni    0.24651552      0.40393467      6.09946491
O     0.25310378      2.21142319      7.17283136
O     0.23973986      3.90597127      5.11644904
H     0.22674532      3.88691776      4.14504379
Ni    -1.32507587     3.12385221      6.11129305
O     -1.37471864     4.78586672      7.02319678
O     4.84473557      1.37876029      5.11451478
H     4.85685689      1.40390616      4.14333712
Ni    3.27964809      0.46507507      6.23967882
O     3.27819645      2.33558727      7.03030733
O     3.27787642      3.96663891      4.79139616
H     3.27070267      3.96752005      3.81960624
Ni    1.81627940      3.12255385      6.10517930
O     1.86797982      4.78434828      7.02027213
H     0.27216915      2.19515695      8.14516930

γ-NiOOH (0001) – oxidised

Cell:

6.065992   0.0   0.0
-3.032996   5.2533066   0.0
0.0   0.0   12.0

xyz-coordinates

| O  | 1.76196071  | 1.31466392 | 5.49761057 |
|----|-------------|------------|------------|
| H  | 1.78588649  | 1.31192120 | 4.52501691 |
| Ni | 0.23609752  | 0.43894696 | 6.59242780 |
| O  | 0.23380086  | 2.18777053 | 7.47429891 |
| O  | 0.24546274  | 3.94131647 | 5.49761025 |
| H  | 0.26938845  | 3.93857447 | 4.52501684 |
| Ni | -1.28040025 | 3.06559847 | 6.59242849 |
| O  | -1.28269708 | 4.81442312 | 7.47430009 |
| O  | 4.79495781  | 1.31466454 | 5.49761031 |
| H  | 4.81888270  | 1.31192136 | 4.52501681 |
| Ni | 3.26909197  | 0.43894607 | 6.59242718 |
| O  | 3.26679856  | 2.18777145 | 7.47430032 |
| O  | 3.27845925  | 3.94131743 | 5.49760996 |
| H  | 3.30238472  | 3.93857460 | 4.52501674 |
| Ni | 1.75259393  | 3.06559775 | 6.59242803 |
| O  | 1.75030098  | 4.81442378 | 7.47430146 |